MINIATURIZED STIRLING ENGINES FOR WASTE HEAT RECOVERY

By

Lacey-Lynne Lemaire

Department of Mechanical Engineering
McGill University
Montréal, Canada

Thesis submitted to McGill University in partial fulfillment of the requirements for the degree of Master of Engineering

Under the supervision of:

Professor Srikar Vengallatore

Department of Mechanical Engineering

McGill University

March 2012

Abstract

Portable electronic devices have made a profound impact on our society and economy due to their widespread use for computation, communications, and entertainment. The performance and autonomy of these devices can be greatly improved if their operation can be powered using energy that is harvested from the ambient environment. As a step towards that goal, this thesis explored the feasibility of developing miniaturized Stirling engines for harvesting waste heat. A mesoscale (palmtop-size) gamma-type Stirling engine, with a total volume of about 165 cm^3, was manufactured using conventional machining techniques. The engine was able to sustain steady-state operation at relatively low temperature differentials (between 20 ^oC and 100 ^oC) and generated a few millijoules of mechanical energy at frequencies ranging from 200 to 500 revolutions per minute. Subsequently, the gamma-type engine was transformed into a Ringbom engine; and its operation was compared with the predictions of an analytical model available in the literature. The experience gained from these studies provides some guidelines for further miniaturization of Stirling engines using microfabrication technologies.

Sommaire

Les appareils électroniques portatifs ont définitivement laissé un impact sur notre société et économie par leur utilisation fréquente pour le calcul, les communications et le divertissement. La performance et l'autonomie de ces appareils peuvent s'améliorer grandement si leur exploitation fonctionne en utilisant l'énergie récoltée de l'environnement. Pour s'orienter vers ce but, cette thèse a exploré si le développement d'un moteur Stirling fonctionnant sur l'énergie résiduelle était faisable. Un moteur Stirling de configuration 'gamma', de la grandeur d'une paume de main, avec un volume d'environ 165 cm^3, a été fabriqué en utilisant des techniques conventionnelles d'usinage. Ce moteur a été capable de soutenir l'opération constante et stable à des différences en température relativement basses (entre 20 ^oC et 100 ^oC). De plus, il a produit quelques milli-Joules d'énergie mécanique à des fréquences entre 200 et 500 révolutions par minute. Par la suite, le moteur Stirling de configuration 'gamma' a été transformé en un moteur Ringbom. Par après, l'opération de ce moteur a été comparée à des prédictions basées sur un modèle analytique disponible dans la littérature. Les informations recueillies durant cette étude ont fourni certaines directives pour la miniaturisation éventuelle d'un moteur Stirling en utilisant des techniques de microfabrication.

Acknowledgements

Above all, I would like to thank Professor Srikar Vengallatore, my supervisor, for his guidance and support throughout my experience as a graduate student. His kindness, keen eye for details, and devotion to helping students grow through their own realizations are things that I will never forget. For that, I extend my sincerest gratitude to him.

I would also like to thank Professor Luc Fréchette from the Université de Sherbrooke and Professor Fabien Formosa from the Université de Savoie for their help during my studies. A kind thank you goes out to Christopher Bisson and François Palucci, two SURE Program students, for their role in the fabrication of a second prototype Stirling engine. In addition, without the funding from NSERC, I would not have been able to pursue this degree.

It was a blessing that my desk was located in FDA-015. This was a space I shared with many wonderful individuals with whom I have countless memories and who have made my time as a graduate student so very precious. I would especially like to thank Nabil Shalabi for opening my eyes to pursuing a master's degree with Professor Srikar Vengallatore. I am grateful for the many discussions shared with Hassan Shahriar. Mostly, I would like to thank my true friend Guruprasad Sosale for putting up with sitting beside me for two years and his countless efforts in keeping me afloat throughout my thesis. He challenged me – in all aspects of my

personal and professional life –, made me laugh, listened when I needed to vent, and offered his advice when I needed to hear it. Now that our lives have led us down different paths, I will miss him terribly.

Furthermore, I would like to thank Chris for his understanding, encouragement, love, and friendship over the years. Lastly, I am thankful for the love and support from my parents and siblings.

Table of Contents

List of Figures

List of Tables

List of abbreviations, designations, and symbols

Abbreviations

MEMS	Microelectromechanical systems
FPSE	Free-piston Stirling engine

Designations

PT2-FBCP	A mesoscale gamma-type Stirling engine
RingStir-L^3	A mesoscale Ringbom engine

Latin symbols

A	Cross-sectional area of a displacer
A_D	Cross-sectional area of a displacer-cylinder
A_f	Area of a flywheel disk
A_p	Cross-sectional area of a piston-cylinder
A_P	Cross-sectional area of a piston
A_R	Cross-sectional area of a displacer rod
B_n	Beale number
C_o	Constant involving certain operating and geometric parameters

f	Frequency of rotation
h	Thickness of a flywheel disk
I	Moment of inertia of a flywheel disk
K	Constant involving certain operating and geometric parameters
L_D	Stroke of a displacer
L_p	Stroke of a power piston
L_P	Amplitude of the motion of a piston
L	Maximum amplitude of the motion of a displacer
m	Mass of a flywheel disk
M	Mass of working fluid
Δp	Difference in pressure across a displacer rod
p	Instantaneous pressure of a working fluid
p_m	Mean pressure during a Stirling cycle
P_{out}	Output power of an engine
R	Gas constant of working fluid
t	Time
ΔT	Temperature differences between a hot and cold surface, ($\Delta T = T_H - T_C$)

T_E	Temperature of a working fluid in the expansion space of an engine
T_C	Temperature of a working fluid in the compression space of an engine
T_D	Temperature of a working fluid in the dead space of an engine
V_c	Instantaneous volume of a compression space of an engine
V_d	Swept volume of a displacer
V_D	Volume of dead space in an engine
V_e	Instantaneous volume of an expansion space of an engine
V_p	Swept volume of a power piston
V_S	Dead space volume
$W_{Schmidt}$	Indicated work per cycle
x_D	Position of a displacer at time, t
x_P	Position of a piston at time, t

Greek symbols

α	Lead of the phase angle of a displacer over a piston

λ	Ratio of the amplitude of the motion of a piston to the maximum amplitude of the motion of a displacer
κ	Ratio of the area of a piston to the area of a displacer
κ_p	Swept volume ratio
κ_S	Dead space volume ratio
ρ	Ratio of the area of a displacer rod to the area of a displacer
ρ_{Al}	Density of aluminum
σ	Dimensionless parameter
τ	Ratio of the temperature of a compression space to the temperature of an expansion space
τ'	Ratio of the temperature of a compression space to the temperature of a working fluid in a dead space
ω	Speed of rotation of the flywheel disk

Chapter 1: Introduction to Stirling engines

1.1 History of the Stirling engine

In 1816, Robert Stirling, a Minister of the Church of Scotland, invented the closed-cycle regenerative engine that eventually took on his name and came to be known as the ‘Stirling Engine’. Throughout the nineteenth century, thousands of Stirling engines were built and used, partly because these were safer than the reciprocating steam-engines of that era. However, these Stirling engines were smaller than steam engines and produced much less power [1].

Stirling engines were widely used up until the first decade of the twentieth century when they were largely replaced by the internal combustion engine and the electric motor. Commercial production of Stirling engines was phased out by the First World War [1]. Nevertheless, many research laboratories have continued to work on these engines ever since. The American Stirling Company offers model Stirling engine kits that can be used as teaching tools. These kits range from small, easy-to-build Stirling engines used primarily as classroom demonstrative tools, to meticulously designed Stirling engine models used for university laboratories [2].

From 1981 to 1987, the Office of Vehicle and Engine Research and Development at the U.S. Department of Energy sponsored the Automotive Stirling Engine Development Program [3, 4]. The aim of the program was to show that the Stirling engine was capable of a 30% increase in fuel-economy over the conventional spark ignition engines for the same class of vehicle and to demonstrate the potential for reduced emissions. This program resulted in one Stirling engine that was suitable for commercial manufacturing and use in automobiles. However, due to the high production costs for specialized tooling to build the Stirling engine and the lack of commercial experience, the Stirling engine was not introduced into the automotive industry.

In 1995, the Swedish navy deployed a Gotland class submarine with the world's first Stirling engine air-independent propulsion system [5, 6]. This system drives a 75 kW generator, which is used for charging the batteries or for propulsion [5]. The Stirling engine is ideally suited for a submarine because the surrounding water can be used as a heat sink, and the engine generates very little noise.

Devices working on the Stirling cycle have also been used for cooling down to cryogenic temperatures and such cryocoolers have been used in space and military applications [7]. The Lanzhou Institute of Physics developed a Stirling cryocooler with a cold cylinder outer diameter of only 6.45 mm and a cooling capability of 0.5 W at 80 K. The lowest temperature that could be achieved by the cryocooler was 52 K [7].

Thus, until recently, Stirling engines have been used mainly for education and for a few specialized applications. This status is slowly beginning to change because of growing interest in renewable energy sources and energy harvesting. Stirling engines can generate mechanical and electrical energy from waste heat and solar radiation without producing any harmful emissions. These attractive characteristics have been exploited by deploying Stirling engines in large arrays for distributed energy harvesting. **Figure 1.1** shows a photograph of one such array from the Stirling Energy Systems solar plant in the Mojave Desert [8]. This concept can be extended to portable devices by developing miniaturized Stirling engines. Indeed, the use of Stirling engines for harvesting waste heat to power portable devices is the application of primary interest for the work presented in this thesis.

Figure 1.1 – Photograph of the Sierra Sun-Tower solar plant at Mojave Desert, USA. Stirling engine waste heat energy harvesters could potentially use solar radiation as a heat source [8].

1.2 Defining characteristics of Stirling engines

To discuss the use of Stirling engines for portable power generation, it would be beneficial to first describe their defining characteristics. The Stirling engine is an external combustion engine and works on the principle of pressure differences inside the cylinders created from external temperature differences. The engine can operate from any number of compressible working fluids. Mechanical power is produced via the closed-cycle expansion and compression of the internal working fluid, which is controlled solely by internal volume changes [9]. The repetition of several thermodynamic processes comprises the 'cycle' which is used to describe the working principles of engines and even characterizes the engines themselves.

1.3 Review of thermodynamic cycles

Before going into the principles of operation of the Stirling engine, it is useful to review some basic features of thermodynamic cycles. The important parameters in the steps of a thermodynamic cycle include entropy (S), pressure (P), volume (V), and temperature (T). These parameters help to explain the processes involved in thermodynamic cycles.

1.3.1 The Carnot cycle

The Carnot cycle is the ideal cycle as all processes are fully reversible, presenting this particular cycle with the highest possible efficiency. To discuss the thermodynamic processes, let us consider a simple system consisting of a single-component ideal gas contained within a piston-cylinder assembly. This piston-cylinder assembly is fully insulated on its sides and can be moved and placed on different surfaces maintained at different temperatures. As shown in the schematic in **Figure 1.2,** there are two thermal reservoirs, one at the cold temperature, T_C, and the other at the hot temperature, T_H. The blue arrows indicate the directions of energy transfer by heat at different stages of this cycle.

First, the piston-cylinder assembly is placed on the cold reservoir. Here, the gas is compressed isothermally and heat is expelled to the cold reservoir, denoted by Q_C. This constitutes process 1-2 on the *P-V* diagram shown in **Figure 1.3**. During this process, the volume under the piston decreases; and the pressure increases slightly as a result. Next, the piston-cylinder assembly is placed on the insulating stand for process 2-3. The gas is further compressed. However, in this process there is no heat transfer. Thus, the compression occurs adiabatically resulting in a large increase in pressure and an increase in temperature to T_H. In the isothermal process 3-4, the assembly is placed on the hot reservoir. As the piston moves upward, allowing the gas to expand, the volume increases, pressure decreases, and heat is transferred into the cylinder such that the gas remains at T_H. Finally, in process 4-1, the assembly is placed once again on the insulating stand. The piston continues to move upward, allowing the gas to expand. This expansion occurs adiabatically, which results in a pressure decrease and a volume increase. The temperature during this process drops until it reaches T_C [10]. The cycle can then begin again from point 1.

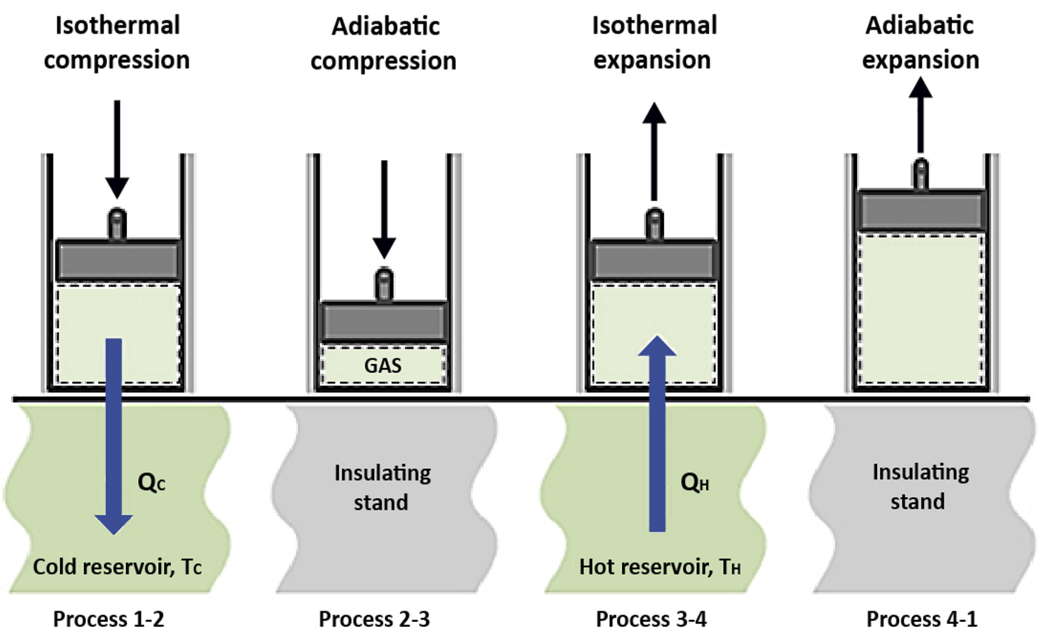

Figure 1.2 – Schematic illustration of the primary processes associated with the Carnot power cycle [10]. The arrow associated with Q_C indicates the direction of heat transfer (from the working fluid to the heat sink). The arrow associated with Q_H indicates the direction of heat transfer (from the heat source to the working fluid).

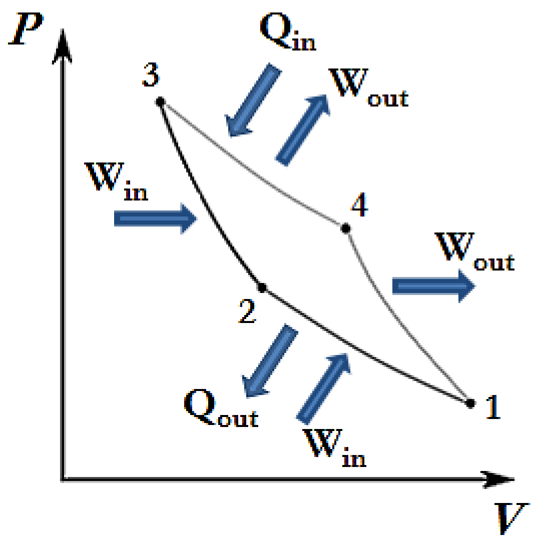

Figure 1.3 – Schematic graph illustrating the changes in pressure (P) and volume (V) for the Carnot cycle. The cycle consists of four processes and these are labeled 1-2, 2-3, 3-4, and 4-1 in the diagram [10].

The efficiency of the cycle is defined as the ratio of the net cycle work produced to the total heat supplied. For the Carnot cycle, the efficiency is given by

$$\eta = \frac{(T_H - T_C)}{T_H}. \quad (1)$$

Unfortunately, this ideal cycle can never be reproduced in any practical engine since no material can perfectly insulate or conduct. There are also non-idealities and irreversibilities associated with friction and leakage losses, which degrade the efficiency of the engine. In practice, however, the Stirling cycle can closely approach the limits established by the Carnot cycle.

1.3.2 Ideal Stirling cycle

A main difference between the Carnot cycle and the Stirling cycle is that there is no adiabatic process in the Stirling cycle. In view of the fact that the working principle of the Stirling engine is internal volume changes of the working fluid, it would suffice to explain the thermodynamic phases which create these volumetric expansions and compressions. There are ideally four thermodynamic processes: two isothermal and two isochoric.

Figure 1.4, modified from the work of Thombare *et al.* [11], shows the *P-V* and *T-S* diagrams, as well as a schematic of an engine configuration, for the Stirling cycle. The engine schematic is a simplified representation of a cylinder containing two opposing pistons. The pistons are separated in space by a regenerator, which is a device for storing thermal energy. One volume is denoted as a *compression space*, maintained at the lower driving temperature, T_C, and the other as an *expansion space*, maintained at the higher driving temperature, T_H. The regenerator, therefore, experiences a thermal gradient because it is assumed that no thermal conduction occurs in the longitudinal direction. This is the ideal case where no friction or leakage losses exist.

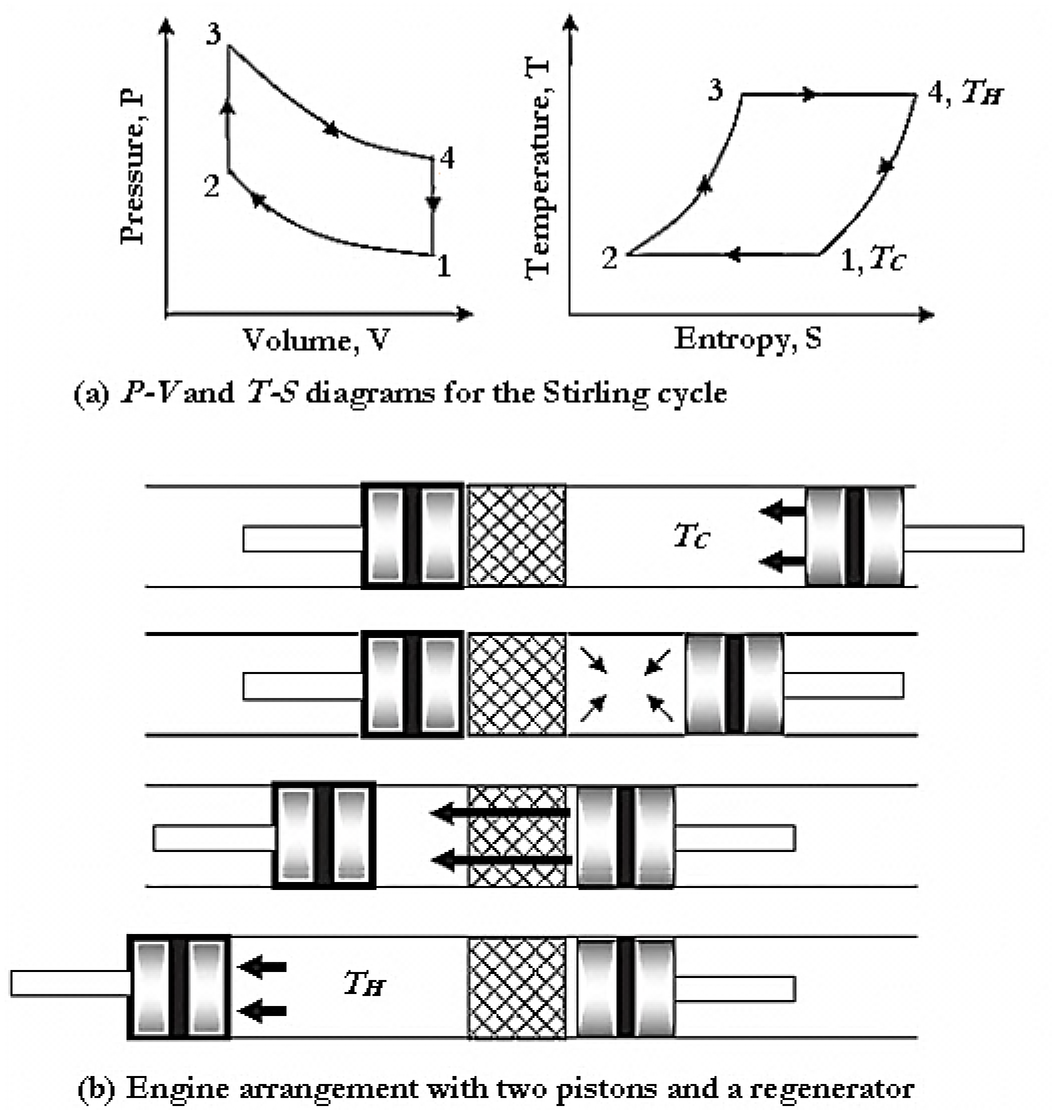

Figure 1.4 – (a) Schematic graphs showing the pressure (P) versus volume (V) relationship and the temperature (T) versus entropy (S) relationship for the Stirling cycle. (b) Schematic representation of a simple configuration for a Stirling engine [11].

Let 1 on the *P-V* and *T-S* diagrams denote the starting position of the cycle. At this location, the piston in the compression space is at the outer dead point and the expansion space piston is at its inner most dead point. Here, the volume of the compression space is at its largest and the temperature and pressure are at their minimum, as can be seen in **Figure 1.4 (a).**

As the compression space piston moves towards its inner most dead point, process 1-2, heat is rejected to the environment and the temperature is held constant inside this volume. This is the first isothermal process. Until the pressure in the compression space reaches a value that is sufficient to displace the expansion space piston, that piston remains stationary.

In process 2-3, the pressure in the compression space is sufficient to displace the expansion space piston towards its outer most dead point. The volume between the two pistons remains constant throughout this process as the two pistons move simultaneously. The regenerator now comes into play. The stored heat from the regenerator is transferred to the working fluid as it passes towards the expansion space volume, increasing the temperature from T_C to T_H.

Increasing the temperature of the working fluid to its maximum and maintaining it throughout the process also increases the pressure inside the expansion volume space. This increase in pressure pushes the expansion space piston to its outer most dead point, while the temperature remains constant at T_H and the compression space piston remains stationary at its inner most dead point. This is represented by the expansion process 3-4 on the P-V and T-S diagrams.

The final process, process 4-1, consists of the expansion space piston moving towards the regenerator and compression space piston away from it, simultaneously. This is the second isochoric process. Therefore, the volume remains constant while the working fluid flows through and transfers its heat to the regenerator. Thus, it emerges in the compression space at T_C. The regenerator now retains that heat until the process begins again when heat is released to the passing working fluid.

The regenerator is imperative in aiding the Stirling cycle to be at its most efficient. If both heat transfer processes have the same magnitude (i.e. heat transferred in process 2-3 is the same as that in 4-1), then the thermal efficiency of the Stirling cycle is the same as that of the Carnot cycle. In practice, however, irreversibilities and non-idealities lead to a degradation of the efficiency.

1.4 Classification of the Stirling engine

The Stirling cycle can be implemented in many different ways. Nearly all implementations make use of a regenerator to have the cycle approach the Carnot cycle as closely as possible, but differ in most other aspects. For example, some implementations make use of two pistons within a cylinder, as illustrated in **Figure 1.4**, while others use a combination of a displacer and a piston. This section discusses the various approaches for classifying Stirling engines.

1.4.1 Types of Stirling engine configurations - α, β, γ, free-piston

There are several arrangements of a Stirling engine. The configurations have a hierarchy of classification in which the mode of operation is most important, followed by the form of cylinder coupling, and, finally, the form of piston coupling [11]. These different approaches for classifying Stirling engines are illustrated in **Figure 1.5.**

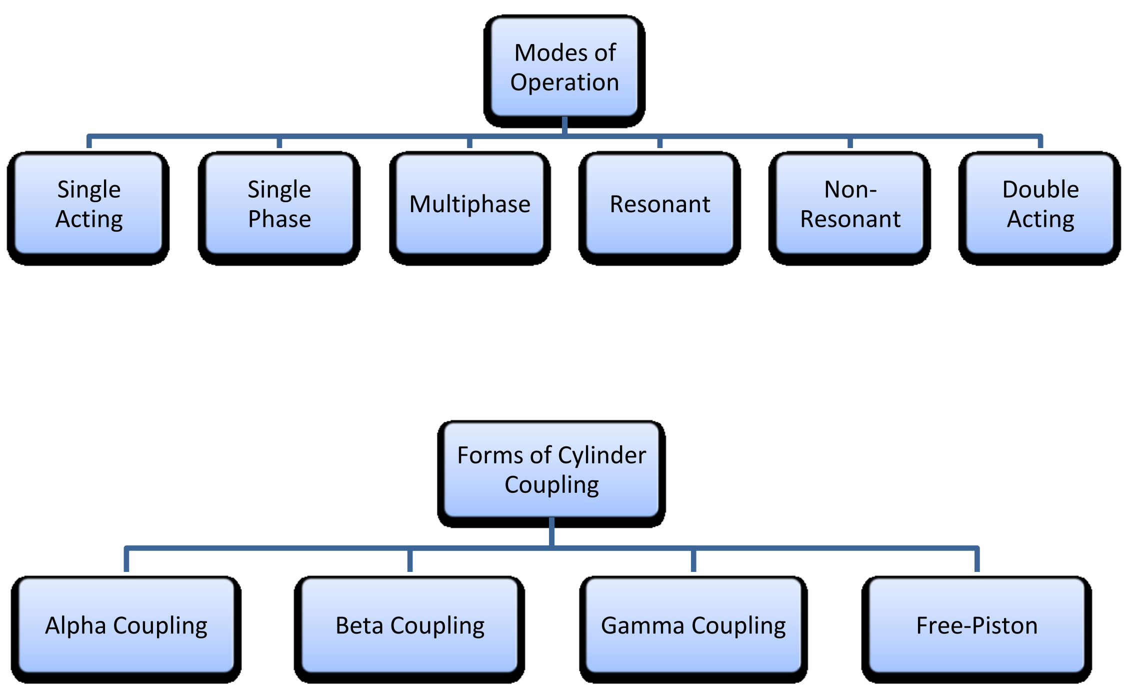

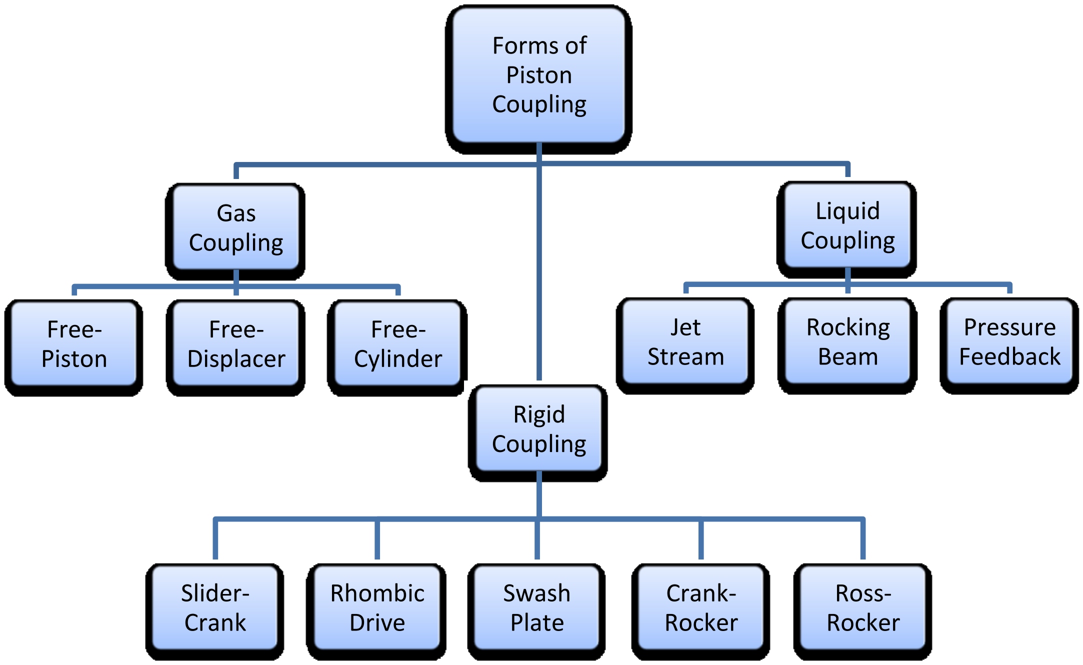

Figure 1.5 – Schematic representation of the i) Modes of operation ii) Forms of cylinder coupling iii) Forms of piston coupling.

Now that a general view of the engine configuration and the cylinder-piston coupling has been presented, a more detailed account of each form of cylinder coupling will be explained. This is a primary focus of research because the results can guide the selection of the optimal type of Stirling engine for the specific application under consideration.

1.4.2 Modes of operation

Stirling engines are mainly classified into two categories based on the mode of operation, namely, *single acting engines* and *double acting engines*. In single acting engines, the working fluid applies a force on only one side of the piston. The fluid can flow through two different cylinders, but the piston only experiences forces from this fluid on one of its sides. The doubling acting engines, on the other hand, have fluid working on both sides of the piston [11].

1.4.3 Forms of cylinder coupling

Alpha configuration

The alpha configuration consists of two separate cylinders each containing its own piston. This is a simple design, as can be seen from **Figure 1.6**, but requires more seals because it has two pistons instead of a single one. With the additional seals, there is more chance of leakage losses which can degrade engine performance.

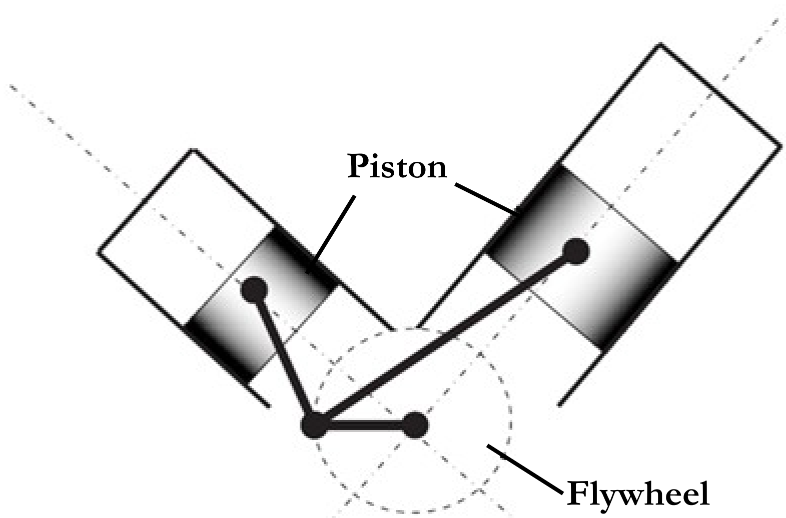

Figure 1.6 – Schematic illustration of the alpha configuration for a Stirling engine [11].

Beta configuration

The beta configuration is the design invented by Stirling and this design has been widely used ever since. In 1871, Schmidt used a beta configuration to develop the first model for the performance of a Stirling engine [12]. The beta configuration has a piston and a displacer in the same cylinder where the compression space of the engine sits in between the top side of the piston and the bottom side of the displacer. The beta design of the engine is shown in **Figure 1.7**.

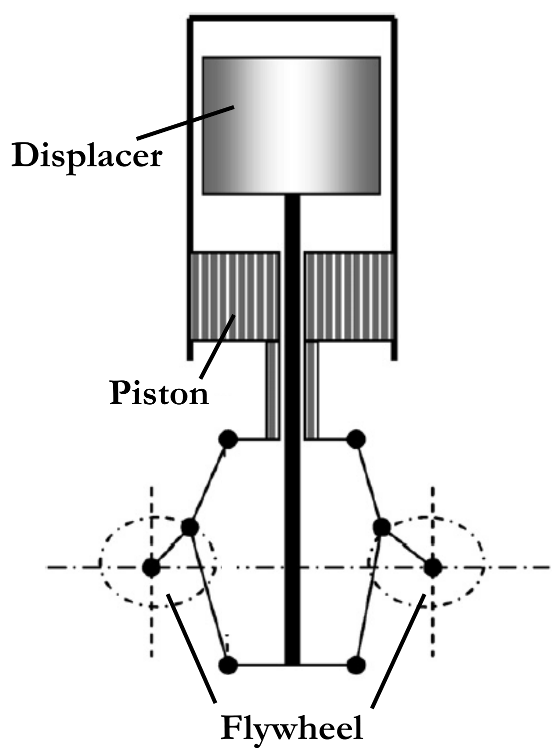

Figure 1.7 – Schematic illustration of the beta configuration for a Stirling engine [11].

Gamma configuration

The gamma-type engine is similar to the beta configuration, differing only in that the piston and displacer are housed in separate chambers, as shown in **Figure 1.8.** The compression space in this arrangement exists in both cylinders. Specifically, the compression space is the air passage port above the piston and below the displacer. The gamma configuration contains a simple crank mechanism, which is a great advantage over other configurations.

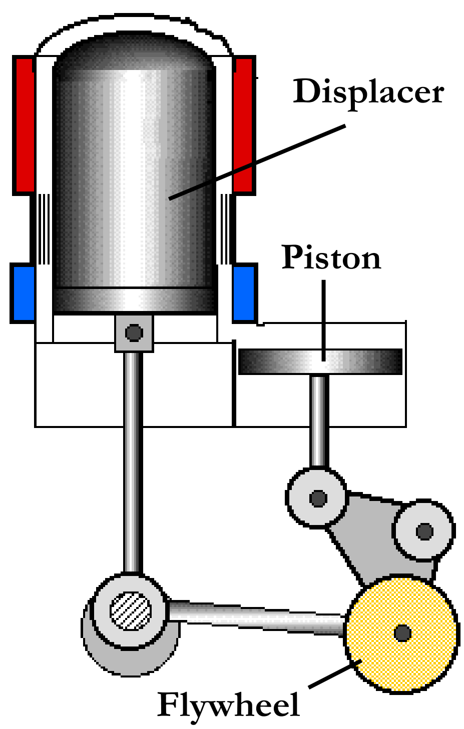

Figure 1.8 – Schematic illustration of the gamma configuration for a Stirling engine [11].

Free-Piston configuration

Although the free-piston Stirling engine (FPSE) is, in essence, a beta configuration [12], this design does not require any mechanical linkages to couple the various component. Free-piston engines consist of a piston and a displacer housed in the same cylinder, as illustrated in **Figure 1.9**, and these components move solely in response to gas pressures or spring forces. Another important aspect is that these engines are self-starting; this feature is something that is not shared with the sister alpha, beta, and gamma crank-controlled engines [1].

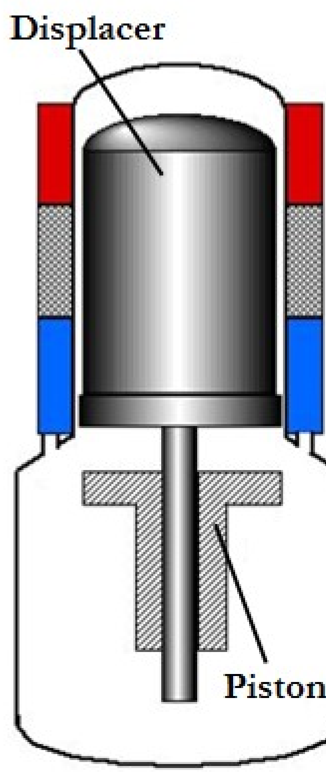

Figure 1.9 – Schematic illustration of the free-piston configuration of the Stirling engine [11].

The free-piston Stirling engine lacks a rotating shaft. This feature is a disadvantage for large-scale (macro) Stirling engines, but may turn out to be particularly advantageous for miniaturization. This issue will be discussed in greater detail in Chapter 4.

1.5 Approaches for design and analysis

The Stirling cycle appears conceptually simple because it avoids the complexities associated with combustion and phase change. This simplicity is rather misleading: the rational design of Stirling engines can be difficult because of numerous challenges associated with analyzing and predicting their behavior. As discussed in Section 1.4, the Stirling cycle can be implemented using multiple types of configurations that employ mechanisms of varying levels of complexity. Furthermore, the operation of these engines involves intricate coupling between fluidic, thermal, and structural domains, and some of these couplings can lead to nonlinear responses.

Taken together, these factors imply that a hierarchy of models with increasing levels of complexity is necessary for design and analysis of Stirling engines. At one end of this spectrum are empirical correlations and rules-of-thumb. These correlations can be evaluated quickly to obtain order-of-magnitude estimates of performance without accounting for the details of design and operating parameters. At the other end are detailed fully-coupled nonlinear models that require considerable computational effort. These models are well suited for detailed design but are inefficient for a rapid exploration of the design space. In between these two limits are scaling analysis that strike a balance between accuracy and computational effort.

A well-known correlation for predicting the power of Stirling engines is the Walker-Beale formula [13]. This correlation can be expressed as

$$P_{out} = B_n \, p_m \, V_p \, f \qquad (2)$$

where P_{out} is the engine power output in Watts, B_n is the Beale number, p_m is the mean cycle pressure in bar, V_p is the volume covered by the power piston in cm^3, and f is the frequency in Hz. The value of the Beale number is usually set to 0.15 based on the performance of a wide range of Stirling engines [9]. Substituting this value into equation (2), the performance of the engine can be calculated using

$$P_{out} = 0.15 \, p_m \, V_p \, f. \qquad (3)$$

This simple formula offers a quick and convenient method for estimating the power of Stirling engines. It can be used with confidence for small excursions in the design space for configurations and sizes that have been extensively explored.

However, the validity and utility of this correlation is less certain when it is extended to fundamentally new design configurations, or when a standard configuration is miniaturized to scales that have not yet been experimentally explored.

The empirical correlations can be refined by accounting explicitly for some important design and operating parameters. A well-known example of such an analysis is the one presented by Schmidt in 1871. The Schmidt analysis leads to compact closed-form expressions for evaluating the indicated work per cycle for the different configurations of Stirling engines [13]. For example, the performance of the gamma-type engine configuration is given by

$$W_{Schmidt} = \pi(1-\tau)p_m V_d \frac{\kappa_p \sin\alpha}{Y + \sqrt{Y^2 - X^2}}, \tag{4}$$

$$X = \sqrt{(1-\tau)^2 - 2(1-\tau)\kappa_p \cos\alpha + \kappa_p{}^2}, \tag{5}$$

$$Y = 1 + \tau + \frac{4\kappa_S \tau}{1+\tau} + \kappa_p. \tag{6}$$

In these expressions, $W_{Schmidt}$ is the indicated work per cycle in Nm, $\tau = T_C/T_H$ is the temperature ratio, p_m is the mean pressure during the cycle in N/m^2, $\kappa_p = V_p/V_d$ is the swept volume ratio, $\kappa_S = V_S/V_d$ is the dead space volume ratio, $V_d = A_D L_D$ is the displacer swept volume in m^3, $V_p = A_p L_p$ is the power piston swept volume in m^3, V_S is the dead space volume in m^3, A_D is the displacer-cylinder cross-section area in m^2, A_p is the piston-cylinder cross-sectional area in m^2, L_D is the displacer stroke in m, L_p is the power piston stroke in m, and α is the phase angle lead of the displacer over the piston in degrees [13].

The formulas that emerge from the Schmidt analysis provide useful insight into the functional dependence of performance on the various design variables. At the same time, they can be inaccurate because of several simplifying assumptions which include isothermal compression, isothermal expansion, and perfect regeneration. These assumptions can be relaxed by developing detailed models that account for coupled effects and nonlinearities. A model developed by Senft [14, 15] is discussed in detail in Chapter 3 of this thesis in connection with the design and analysis of a Ringbom-type Stirling cycle engine.

Finally, the effects of size on performance can be explored using scaling analysis. This is an issue that is directly relevant for the applications considered in this thesis, as discussed in the next section.

1.6 Miniaturized Stirling engines

The need for portable energy generation is growing as our society continues to use ever-increasing numbers and types of portable gadgets. Electrochemical batteries are currently the only source for powering portable devices used for computing, communications, and entertainment. Batteries are a mature technology; therefore, improvements in performance occur only in rather small increments at this stage. For some devices, the performance and lifetime of the battery is the primary barrier on the path towards improved performance. Other applications, such as wireless networks of sensors, cannot rely upon batteries. These networks may employ thousands of sensors that are deployed in environments that are either inhospitable or inaccessible. Therefore, changing or recharging electrochemical batteries is not an option for such applications [16, 17]. For all these reasons, there is growing interest in developing new methods for portable power generation.

The demand for portable power ranges from a few microwatts for some types of sensors to about 1 W for cell phones. Some of these devices have to operate in benign conditions but others are deployed in harsh environments. Even at this early stage in the development of this field, it is clear that no single device can meet all these requirements. Therefore, there is value in developing an array of approaches for portable power. This thesis focuses on establishing guidelines for the miniaturization of Stirling engines. For convenience, we can categorize the size of these miniaturized engines as *mesoscale* (palmtop size) or *microscale* (system volume of about 1 cubic centimeter).

Attempts to develop microscale Stirling engines began about twenty years ago. In 1989, Nakajima *et al.* [18] studied the effects of miniaturization on the performance of a Stirling engine using scaling analysis. They then fabricated a mesoscale Stirling engine with a piston swept volume of about 0.05 cubic centimeter. This engine weighed 10 grams and could deliver 10 mW of power. Through computer simulations, it was noted that the flywheel mechanism had a miniaturization limit of 9 mm before it became ineffective.

In 1998, Peterson [19] presented a detailed scaling analysis of regenerative heat engines and came to the conclusion that the lower size limit of a regenerative heat engine was approximately 1 mm. This limit was set to maintain a thermal efficiency above 50% of the Carnot efficiency [19].

Wang *et al*. [20] introduced the use of magnets, coils, and flexible membranes for potential use in small-scale Stirling engines. These approaches offer a route for converting the mechanical energy in the Stirling engine into electrical power. In other words, electromagnetics can be combined into a Stirling cycle engine and a mechanical-electrical converter can be developed. A working prototype of this kind of Stirling engine has not yet been reported.

In summary, a few research groups have explored some aspects of the miniaturization of Stirling engines, but many questions remain open. First, what are the optimal configurations for miniaturization? Second, what are the optimal component sizes for these configurations? Third, how do the limitations imposed by the current state-of-the-art in microfabrication technologies affect the design of miniaturized Stirling engines? The goal of this thesis is to explore some of these questions.

1.7 Aim, approach, and organization of the thesis

The primary aim of this thesis is to establish some guidelines for the miniaturization of Stirling engines for waste heat recovery.

As the first step towards this goal, a gamma-type mesoscale Stirling engine was instrumented and tested. The results of these experiments are described in Chapter 2. Next, the design and analysis of mesoscale Stirling engines was considered in detail. Specifically, a model developed by Senft [14] was used to guide the conversion of the mesoscale gamma-type Stirling engine into a mesoscale Ringbom engine. These details are discussed in Chapter 3. Finally, Chapter 4 consolidates the experience gained with the mesoscale engines to develop some guidelines for the development of microscale Stirling engines.

Chapter 2: Design and testing of a gamma-type Stirling engine

2.1 Design of a gamma-type Stirling engine

This chapter describes the design, instrumentation and testing of a mesoscale gamma-type Stirling engine. This type of engine was selected because it is capable of operating even for small temperature differences, ΔT, between the hot and cold surfaces $(\Delta T = T_H - T_C)$. This feature is particularly appealing for waste heat recovery from a variety of different sources of which some are of relatively low quality. During the summer of 2009, two undergraduate students, François Bisson and Christopher Palucci, designed and constructed two low temperature differential, gamma-type Stirling engines. The smaller of these two engines has a volume of about 165 cm^3. This mesoscale gamma-type Stirling engine, which shall be referred to as the PT2-FBCP engine hereafter, was selected for instrumentation and testing.

The primary components of the engine are the displacer, piston, crank mechanism and flywheel. The relative sizes and locations of these components are indicated in the schematic shown in **Figure 2.1**. The displacer, which is in the form of a thin disc, is housed within a cylindrical chamber. The base plate and top plate seal the displacer chamber and serve as the hot and cold surfaces, respectively, during operation. The piston is also located within a cylindrical chamber that is attached to the top plate. The crank mechanism provides a mechanical connection between the displacer chamber and the flywheel. **Figure 2.2** illustrates the shape and position of the connecting rod of the displacer. This figure also depicts the size and location of the regenerator, which is housed within the disk-shaped displacer.

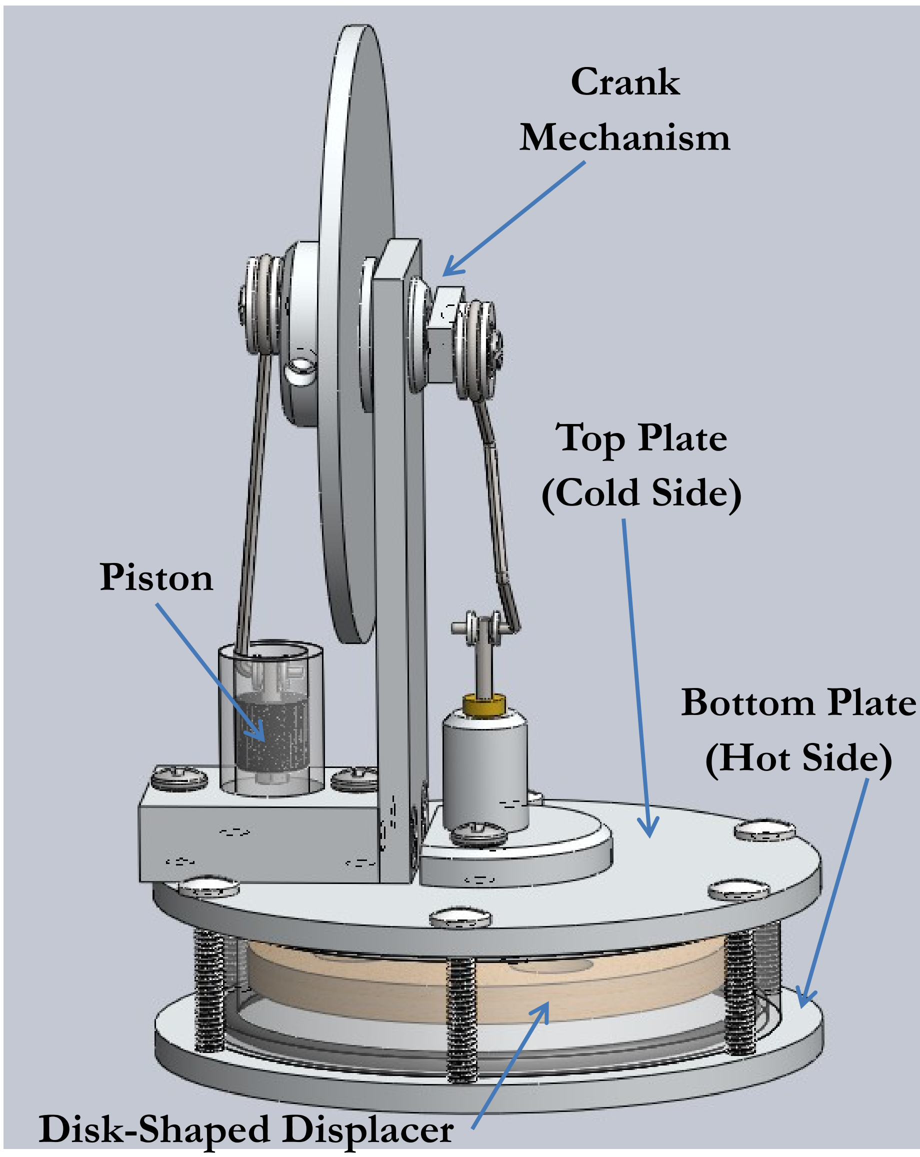

Figure 2.1 – A CAD illustration showing the side view of the PT2-FBCP engine.

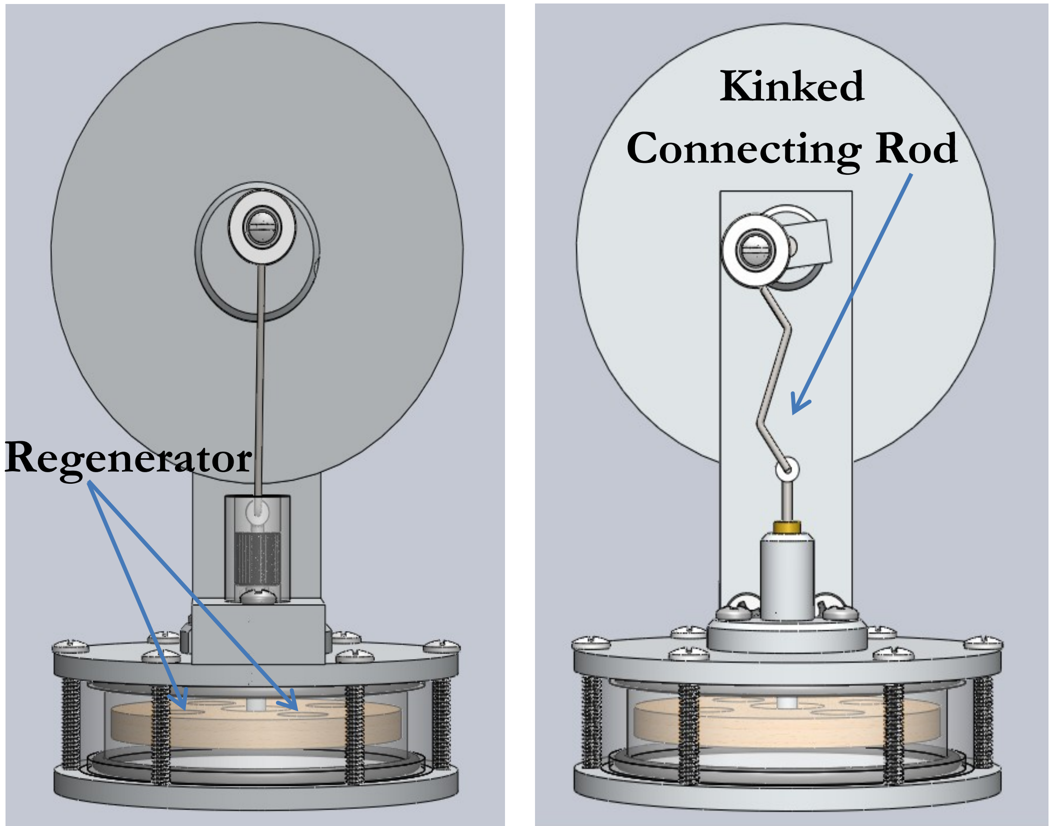

Figure 2.2 – CAD illustrations showing the view of the front (left) and the view of the back (right) of the PT2-FBCP engine. The regenerator is held within the four holes fabricated in the disk-shaped displacer. The shape of the connecting rod minimized transverse motion of the displacer rod.

The design of the PT2-FBCP followed guidelines established by Senft [21]. The compression ratio must be small for the engine to operate from a low ΔT. In turn, this requirement imposes some conditions on the size and shapes of the various components of the engine. First, the swept volume of the displacer, which is the product of the area of the displacer and its stroke, must be much higher than that of the piston. As a rule-of-thumb, the swept volume of the displacer must be roughly fifty times that of the piston. Increasing the swept volume of the displacer by increasing its stroke can lead to large frictional losses. Therefore, the displacer was designed so that it has a large area and a relatively short stroke.

These guidelines were used to identify materials for the various components of the engine. The base plate and top plate must have high thermal conductivity and sufficient rigidity. Therefore, aluminum was chosen to machine these two plates. In contrast, both the displacer and the cylindrical sidewalls of the displacer chamber are required to exhibit low thermal conductivity. In addition, the weight of the displacer must be minimized. Therefore, this disc was machined using balsa wood with foam inserts that served as the regenerator. The cylindrical sidewalls were machined using a transparent polycarbonate material that makes it possible to observe the motion of the displacer during operation.

The piston and piston-cylinder were purchased from Airpot Corporation. The piston-cylinder is precision-bore Pyrex, and the piston is made from graphitized carbon. These materials were chosen because the piston-cylinder set has excellent sealing properties and friction is extremely low [15]. A similar consideration guided the selection of materials for the crank mechanism; brass bushing bearings were selected for this component. The displacer rod, piston rod, and crank shaft were machined using steel and the flywheel was machined using aluminum.

The scale of the PT2-FBCP was set by selecting the diameter of the top plate and base plate to be 5 cm. The height of the engine (that is, from the base plate to the top of the flywheel) is 8.5 cm. **Figure 2.3** shows a photograph of the PT2-FBCP engine. The Appendix contains the detailed, exploded view CAD drawing for this engine. To characterize the performance capabilities of this engine, the next undertaking was to instrument the engine for testing.

Figure 2.3 – Photograph of the PT2-FBCP Stirling engine.

2.2 Instrumentation of the PT2-FBCP engine

The goals for testing the PT2-FBCP engine were to obtain experience in performing experiments with mesoscale Stirling engines and explore their transient and steady-state operation. The engine was instrumented to measure the temperatures of the hot and cold surfaces, and the speed of rotation of the flywheel. The temperature of the base plate was controlled between 30 ^{o}C and 150 ^{o}C by placing it on a heater (Corning stirrer/hotplate). The top plate was exposed to the ambient environment. The temperature of these surfaces was monitored with a precision of $\pm$2 ^{o}C using thermocouples (type-K Omega Chromel-Alumel thermocouples) connected to a multimeter [22].

The thermocouples were attached to the surfaces of the engine using 50 μm thick heat resistant tapes (Flashbreaker 1, AirTech International). The tapes are rated to withstand temperatures of up to 204 ^{o}C [23].

A CASIO EX-F1 high-speed digital camera was used to capture videos of the operation of the engine. This camera offers a video recording capability from 60 to 1200 frames per second (fps). During the tests, videos were recorded at 300 fps. At this setting, the resolution is 512 x 384 pixels. This is slightly less than the standard of 640 x 480 pixels at 30 fps [24], however, still adequate for proper viewing. The camera was set on a tripod stand and a spot lamp was directed towards the engine to provide sufficient illumination.

2.3 Protocols for testing

The experiments consisted of setting the PT2-FBCP engine on the heater, initially at some temperature, $T_{hotplate}$, and allowing the engine to run while being filmed with the high-speed camera. The temperature of the cold surface was not actively controlled but simply exposed to the ambient, which was at a temperature of about 25 ^{o}C. Preliminary tests showed that the engine was not capable of sustained operation unless the temperature of the heater was at least 50 ^{o}C. Therefore, experiments were conducted by varying the temperature of the heater from 50 ^{o}C to 150 ^{o}C in increments of ten degrees. The upper end of this range is set by the fact that the polycarbonate material used for the cylindrical sidewalls of the displacer chamber cannot withstand temperatures in excess of 150 ^{o}C [21].

For each test, the heater was first permitted to reach the desired temperature. The initial temperatures of the base plate and top plate of the PT2-FBCP engine, and the ambient room temperature, were recorded using thermocouples. Subsequently, thermocouples were taped to the base plate and top plate of the engine; and the engine was placed on the heater. A timer was started and the temperature of the base plate was monitored until it reached that of the heater. The engine sat idle during this period.

Once the base plate reached $T_{hotplate}$, the engine was set into operation by gently displacing the flywheel by a few degrees. This was necessary because this type of

Stirling engine is not self-starting. **Figure 2.4** shows a photograph of the engine right before the flywheel was to be set in motion. The PT2-FBCP engine was allowed to run for two minutes and then removed from the heater. All components of the engine were cooled down to room temperature before any further testing.

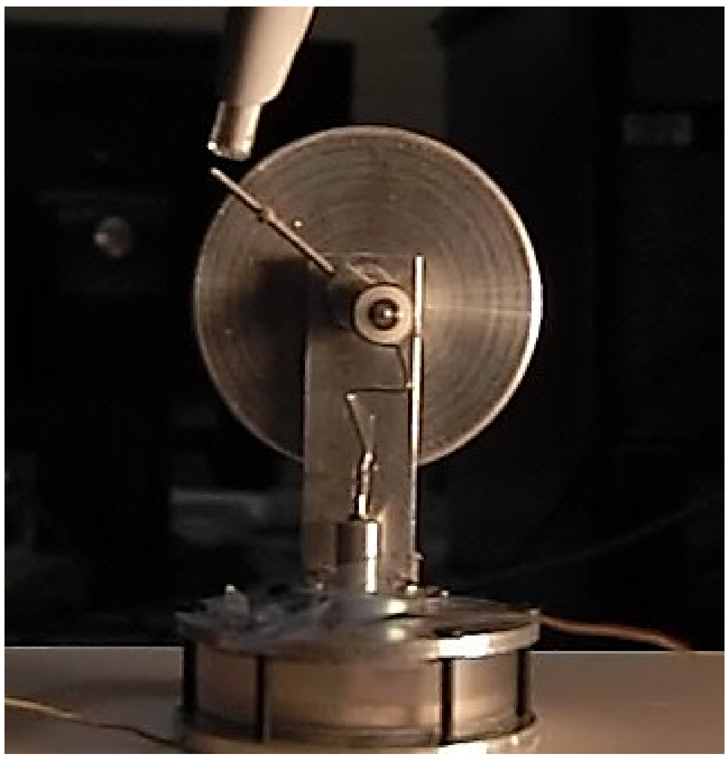

Figure 2.4 – Photograph displaying the PT2-FBCP engine on its test platform at the instant before the flywheel was push-started to set the engine into motion. The flywheel was set in motion by giving it a small tap. It was always started from the position shown.

The speed of the engine, in RPM, was obtained from the videos recorded for each test. The time it took for the flywheel to make one revolution was extracted from the film at four locations in time after the engine reached steady-state, and then the average speed of the flywheel was deduced. To calculate the time for one revolution, the frame number at the starting location in the video of the test was subtracted from the frame number after one revolution. Once this information was obtained, and with the knowledge that the videos were recorded at 300 fps, the speed of the flywheel in revolutions per minute (RPM) was realized.

2.4 Results

2.4.1 Determination of the operating temperature range

During the experiments, the temperature of the hot side of the engine reached the target temperature of the heater to within a few degrees. Heat conduction through the cylindrical sidewalls of the displacer chamber caused the top aluminum plate, the cold side of the engine, to increase in temperature. During the tests with targeted temperatures of the heater from 50 ^oC to 90 ^oC, the heat conduction and increase in temperature of the top plate was not that substantial. However, when the engine was tested at higher targeted temperatures of the heater, the conduction through the cylindrical sidewalls was considerable. For example, the temperature of the top plate increased from the ambient temperature to ~ 50 ^oC when the engine was tested at a target temperature of 150 ^oC.

Table 2.1 presents the targeted temperature of the heater, and it lists the measurements of the temperature of the hot plate and cold plate of the engine. It also shows the ΔT for each test.

Table 2.1 – Table presenting the target temperature of the heat source, $T_{hotplate}$, the average actual temperature of the hot side, $T_{hotside}$, the average temperature of the cold side, $T_{coldside}$, and the corresponding ΔT.

Target $T_{hotplate}$ (°C)	Average Actual $T_{hotside}$ (°C)	Average Final $T_{coldside}$ (°C)	Average ΔT (°C)
50	54.5	31.5	23.0
60	60.0	33.0	27.0
70	72.5	36.3	36.2
80	80.6	37.5	43.1
90	89.6	38.1	51.5
100	100.3	39.5	60.8
110	110.5	40.4	70.1
120	121.9	43.4	78.5
130	133.0	45.7	87.3
140	140.1	46.1	94.0
150	149.9	49.7	100.2

The PT2-FBCP engine was capable of operating on a ΔT in the range of roughly 23 ^{o}C to 100 ^{o}C. In addition, the cold surface of the engine ranged from approximately 30 ^{o}C to 50 ^{o}C when the hot side was tested at 50 ^{o}C to 150 ^{o}C, respectively. This, indeed, does classify the engine as a low temperature differential engine. Although the temperature range of operation seems quite promising for waste heat recovery, a potential problem is the fact that significant heat conduction through the top plate occurs at the higher operating temperatures.

2.4.2 Determination of a standardized and sufficient period of time for testing

Next, a sufficient and standardized time to let the engine operate once the flywheel was set in motion was determined. This was done to insure that the engine reached steady-state, defined as the period in time when the properties are unchanging [10], during each test.

The transient or start-up period of operation of the PT2-FBCP engine was determined using the same test setup mentioned previously. One test to find the start-up time of the engine was performed at each ten degree increment in temperature from 50 ^{o}C to 150 ^{o}C. Therefore, the hot side of the engine spanned this same temperature range; and the temperature of the cold side varied from 30 ^{o}C to 50 ^{o}C, correspondingly. For each of the tests, the high-speed video was used to establish the transient period of operation by measuring the speed of the shaft at every second until a plateau was reached. For one test performed with the temperature of the heater set at approximately 50 ^{o}C, the transient period of operation was not more than ten seconds, as can be seen in **Figure 2.5**. In **Figure 2.6**, the start-up time for the PT2-FBCP engine, with the temperature of the heater set at 150 ^{o}C, was only 4 seconds. These figures also depict the start of a stable area of operation, where the speed of the shaft begins to remain virtually unchanged with time.

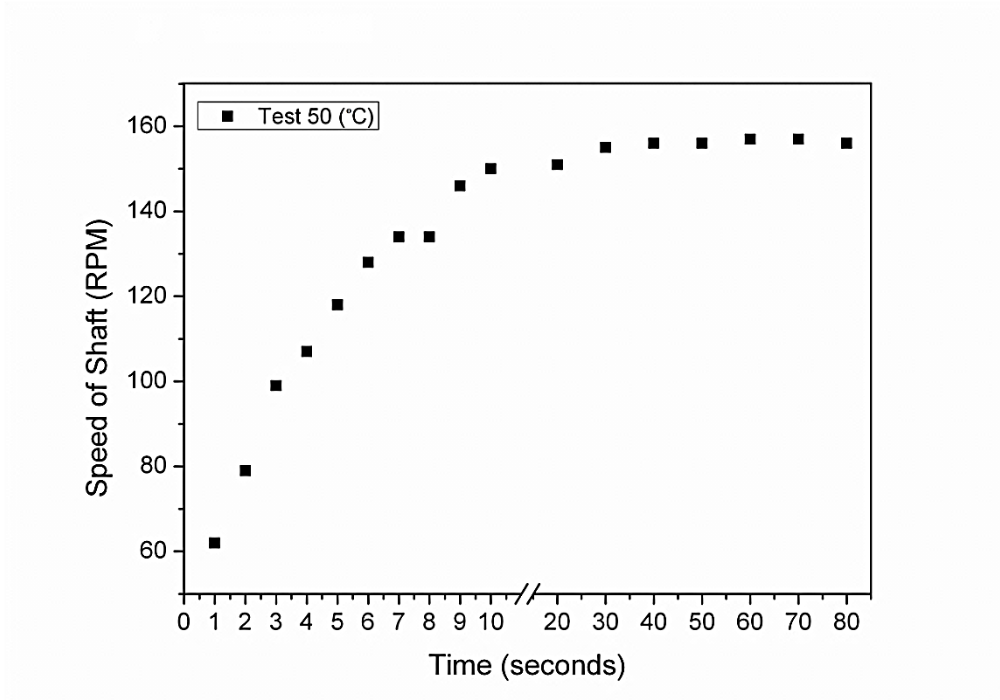

Figure 2.5 - Graph representing the variation of the speed of the shaft with time for a test performed with a heater temperature of roughly 50 °C. The transient region is only a short period in time, ranging not more than ten seconds, after which steady-state is maintained.

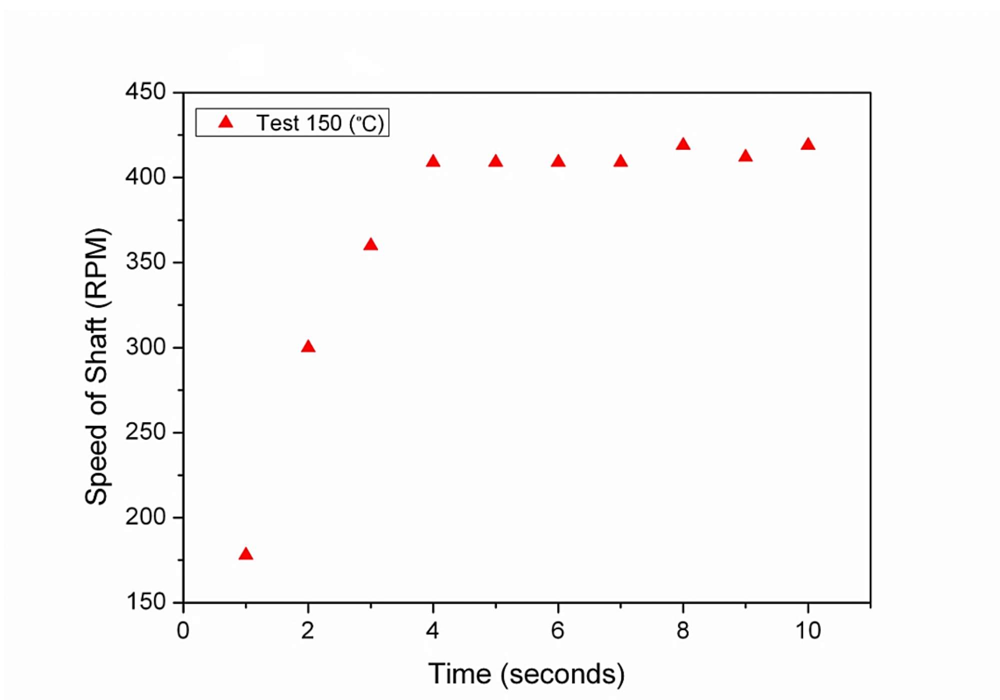

Figure 2.6 - Graph representing the variation of the speed of the shaft with time for a test performed with a heater temperature of about 150 °C. The transient region is much smaller than that of the test with a heater temperature of 50 °C, namely approximately four seconds.

To be certain steady-state was achieved for all the tests performed, a standard time for testing was established. The time period of one of the initial experiments is represented in **Figure 2.7**. This is to show that stopping the tests at the two minute mark is viable and allows the engine to fully complete its transient period of operation and reach steady-state operation.

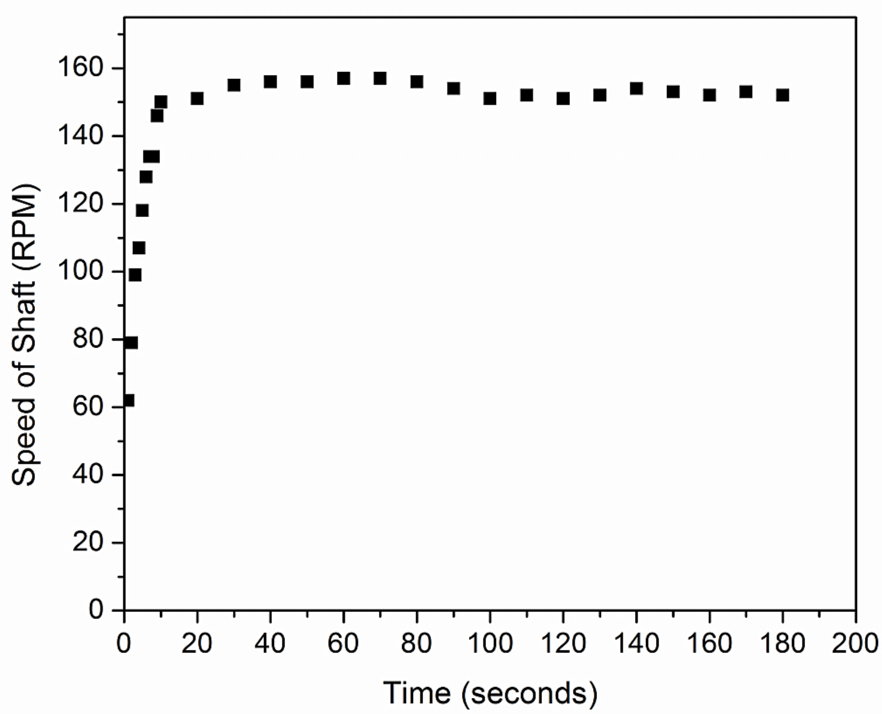

Figure 2.7 – Graph representing the variation of the speed of the shaft with time for a test performed with a heater temperature of approximately 50 °C. The transient region is only a short period in time, ranging not more than ten seconds. Steady-state is clearly obtained after this transient state. The speed of the shaft was not affected by the slight changes in ΔT, which ranged from 18.5 °C to 20.5 °C, throughout the time of the test.

The transient period of operation for the tests done in this thesis was determined to be very short. As shown, the transient time ranged from four to ten seconds for a heater temperature of 150 ^{o}C and 50 ^{o}C, respectively. Furthermore, the PT2-

FBCP engine was allowed to reach steady-state operation before each test was completed. The speed of the engine was measured from this steady-state region of operation.

2.4.3 Determination of the speed of the shaft and the available kinetic energy of the PT2-FBCP engine

Once more, the same test setup was used to explore the performance of the PT2-FBCP engine. It was previously established that the engine would be tested within a heater temperature range of 50 ^{o}C to 150 ^{o}C, inclusive. The average difference in temperature between the hot surface and cold surface of the engine for each of the tests are those listed in **Table 2.1**. Eight tests were performed at each ten degree increment in temperature within the prescribed heater temperature range. This was done to ascertain the repeatability of the experiments.

The high-speed videos were used to measure the angular speed of the shaft and to determine the available kinetic energy output of the engine once it was in a period of steady-state operation. Once the speed of the shaft was obtained from the video, the kinetic energy was calculated from the measurement of the speed of rotation of the shaft using

$$Kinetic\ energy = \frac{1}{2} I\omega^2 \tag{7}$$

where ω is the speed of rotation of the flywheel and I is the moment of inertia of the flywheel. The moment of inertia of the flywheel was obtained using

$$I = \frac{1}{2} m r^2 \tag{8}$$

where m is the mass of the flywheel disk and r is the radius. The mass of the flywheel was obtained by

$$m = \rho_{Al} A_f h . \tag{9}$$

In this expression, m is the mass of the flywheel, ρ_{Al} is the density of aluminum, A_f is the area of the flywheel disk, and h is its thickness.

The PT2-FBCP engine was able to operate for a ΔT as low at 23.0 ^{o}C and as high as 100.2 ^{o}C. From **Figure 2.8**, it can be seen that the engine speed increases with the increase in ΔT. The average minimum and average maximum speed of the flywheel was determined to be 162 RPM and 498 RPM, respectively. **Figure 2.8** also depicts the trend of the kinetic energy available from the shaft in relation to ΔT. Since the engine would not operate at lower temperature differences and could not be run at higher temperatures due to risk of damages, extending the data points beyond the range presented is not possible.

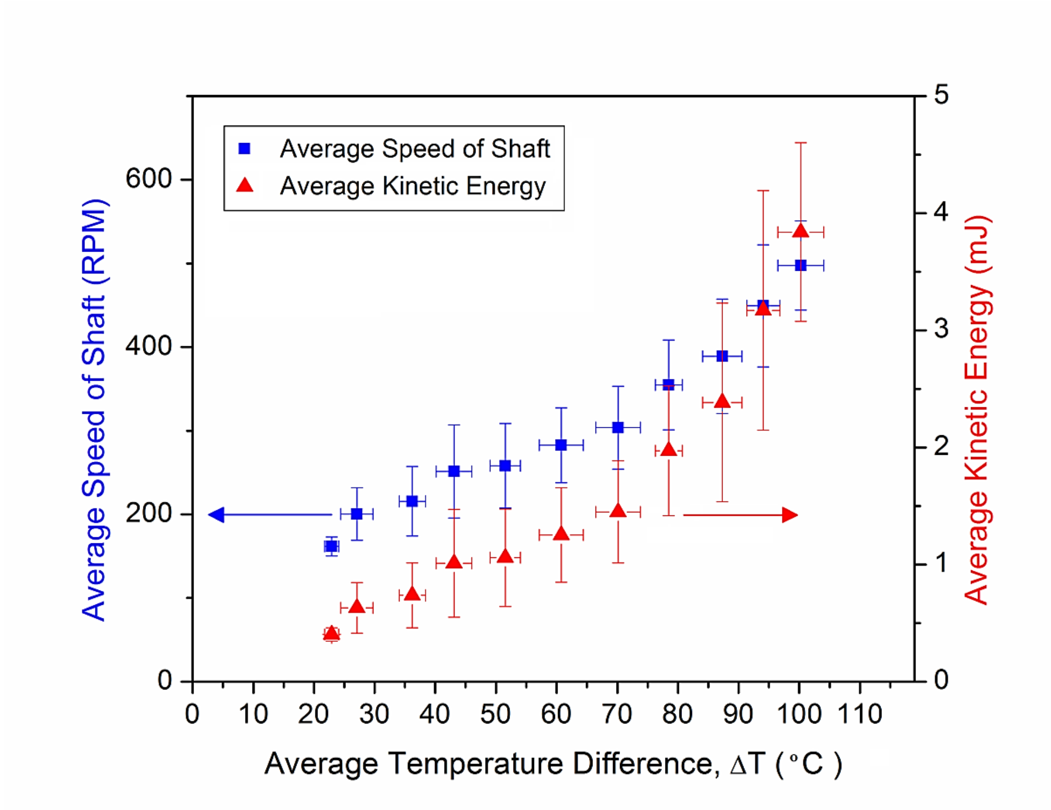

Figure 2.8 – The graph shows the average speed of the shaft of PT2-FBCP engine in relation to the average ΔT between the hot side and cold side. The graph also illustrates the increase in kinetic energy with increasing ΔT.

At its maximum operating ΔT of 100.2 ^{o}C and maximum speed of the shaft of 498 RPM, the PT2-FBCP Stirling engine had 3.84 mJ of kinetic energy available. The energy density of the engine, at its highest operating ΔT, was 0.023 mJ/cm^3.

2.5 Summary

Examining the performance of the PT2-FBCP engine led to a few critical results. For one, the gamma-type mesoscale Stirling engine is not self-starting. This raises the issue of the engine requiring a method of manual start-up. The temperature range of operation for the PT2-FBCP engine was determined to be roughly 50 ^{o}C to 150 ^{o}C. Moreover, the working ΔT of the engine was approximately 23 ^{o}C to 100 ^{o}C due to the heat conduction through the cylindrical sidewalls of the displacer chamber. The speed of the shaft and available kinetic energy were sizeable considering such a low operating temperature differential. The greatest speed of the shaft obtained was roughly 500 RPM. The kinetic energy output associated with this speed was approximately 4 mJ.

With the PT2-FBCP engine tested and its performance documented, the next step was to create another engine taking one step closer to being suitable for micro-design. Designing for microfabrication meant ridding the engine of some linkages. The first phase was focused on only changing one parameter. The simple and obvious choice was to remove the displacer from the flywheel and have it move freely. This would result in the piston still being connected to the crank; however, it would leave the displacer free of connections and its motion no longer associated with the flywheel's rotation. Therefore, the next design step was to create a Ringbom Stirling cycle engine.

Chapter 3: A mesoscale Ringbom engine

3.1 The relation of the Ringbom engine to the Stirling engine

The first Ringbom engine was built by Ossian Ringbom in 1907 [14], some 91 years after the Stirling engine made its debut. The engine operates on the Stirling cycle, using gas pressure from thermal expansion and compression to move both its piston and displacer. Mechanically, the Ringbom engine is closely related to the design of a simple gamma-type Stirling engine. However, the significant difference between the two engines is the connection and interaction between the piston and displacer. As noted earlier, the gamma-type Stirling engine has mechanical linkages that connect the displacer and piston to the flywheel. In contrast, the Ringbom engine has a free-displacer (that is, the displacer no longer has any mechanical linkages), but the piston is still connected to a flywheel. This chief difference entitles the Ringbom engine to its own designation. The features of the engine are illustrated in **Figure 3.1**.

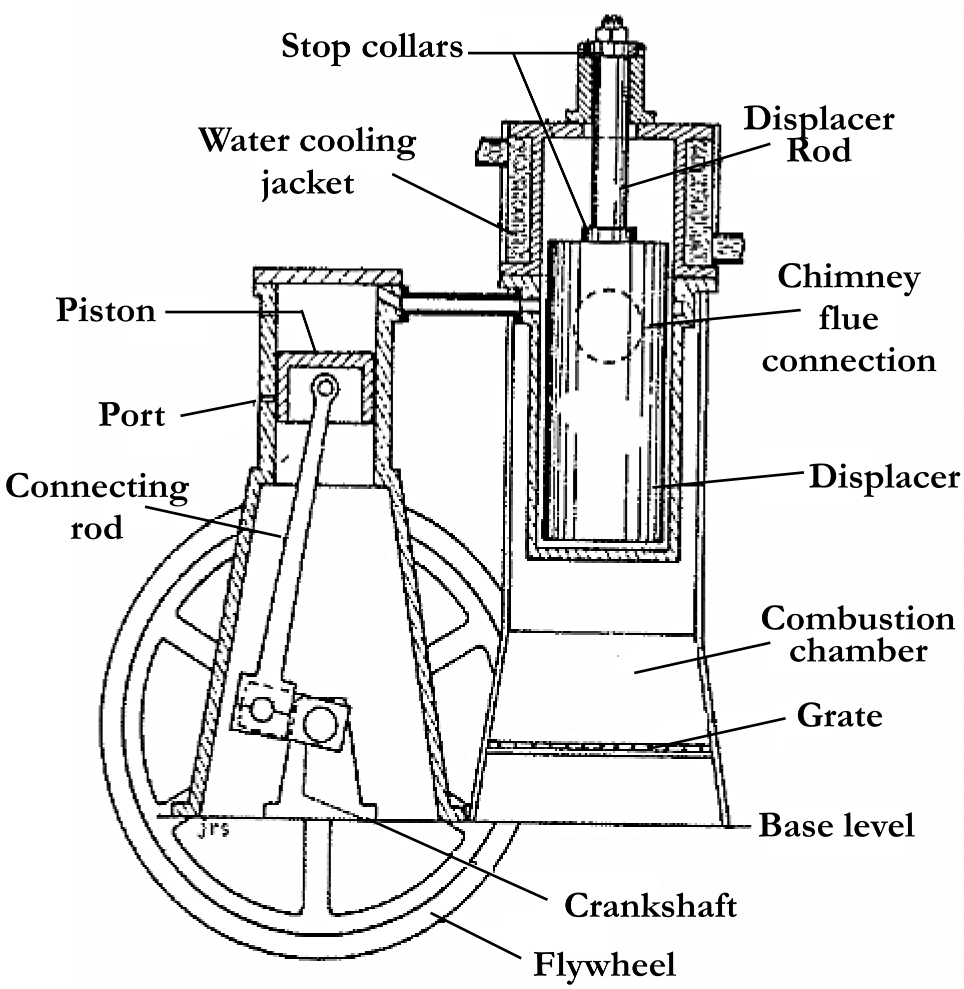

Figure 3.1 – Illustration of the Ringbom engine of Ossian Ringbom [14].

With the piston and displacer no longer linked through the flywheel in the Ringbom engine, the relative motion of these two components cannot be adjusted through altering mechanisms. Therefore, the speed of the shaft, pressure of the working fluid, and operating temperature are the parameters that now control the relationship between the motion of the piston and the motion of the displacer. Optimizing these factors for stable operation can be daunting because multiple parameters must be modified simultaneously to achieve the desired results. A useful starting point is to consider analytical models that can identify the critical parameters that should be modified for stable operation.

3.2 Senft's analytical model for stable operation of mesoscale Ringbom engines

In 1985, Senft [14] published a paper titled "*A mathematical model for Ringbom engine operation*," in which he presented an analytical model for the dynamics of this class of Stirling engines. The primary goal of this model was to identify the set of design and operating parameters that control the 'overdriven mode operation' of a Ringbom engine. In this context, overdriven mode operation is defined by Senft [14] as, "…operation in which the displacer contacts its physical travel limits before the gas pressure difference across its rod changes sign to oppose the motion."

In other words, this mode of operation is steady-state operation with dwell periods. These dwell periods characterize the type of operation of the Ringbom engine. The motion of the displacer is stopped by changes of the gas pressure, which leads to an acceleration that opposes the motion. During a short period of time, the displacer remains motionless until the gas pressure across the displacer rod changes sufficiently to initiate motion and force the displacer in the opposite direction.

3.2.1 Description of overdriven mode operation

The model presents the mathematical expressions involved in determining overdriven mode operation. Such equations outline and establish the characteristics an engine should exhibit in order to operate in this manner. It was demonstrated that a modified Ringbom engine, with the omission of the port located in the piston-cylinder wall shown in **Figure 3.1**, could run off gas pressure differences alone. With the engine now sealed from the outside atmosphere, the mean cycle pressure would then be roughly equal to the external pressure surrounding the engine. Of course, this assumes some leakage past the piston-cylinder assembly and the displacer rod gland. In addition, with appropriate engine geometry, gravity could be neglected.

To better understand overdriven mode operation, the motion of the piston and of the displacer of the engine is represented in **Figure 3.2**. It is assumed for simplicity, and as an arbitrary starting point, that the cycle begins with the piston moving toward its top dead center during its compression stroke. Meanwhile, the displacer sits at the hot end of the engine. The motion of the piston is assumed to be a sinusoidal function of time. Since the internal engine pressure is comparable to the external pressure, the displacer will remain in the hot end of its cylinder until the piston moves far enough into its compression stroke so as to balance the internal pressure of the engine and the external pressure on the displacer rod. This occurs at point ‘a’ on the flywheel, as shown in **Figure 3.2(a)**. At this point, the pressure difference across the displacer rod falls to zero. Once the piston moves beyond this point and the engine enters into its transfer stroke, the pressure within the engine increases due to the increase in temperature of the working fluid. This allows the displacer rod to overcome the external pressure and move away from its hot end toward its cold end. It is assumed that the displacer stops instantaneously at the end of its motion. Therefore, pressure forces are the only forces present acting on the displacer. The expansion stroke consists of the piston being pushed toward its bottom dead center. During this motion, the displacer remains at its cold end; and the internal pressure of the engine drops. At the end of this stroke, the pressure is equal to the atmospheric pressure. Lastly, when the piston passes point ‘b’ in **Figure 3.2(d)**, the pressure of the working fluid in the engine drops below the surrounding pressure. Therefore, the pressure on the displacer rod is greater from its surroundings and pushes the displacer back toward its hot end. The cycle can then begin again with the piston moving through its compression stroke and the displacer at its hot end. One important observation is that the displacer travels through a complete stroke before the position of the piston changes sufficiently to alter the pressure of the working fluid to set the displacer back in motion. This is the fundamental principle of overdriven mode operation.

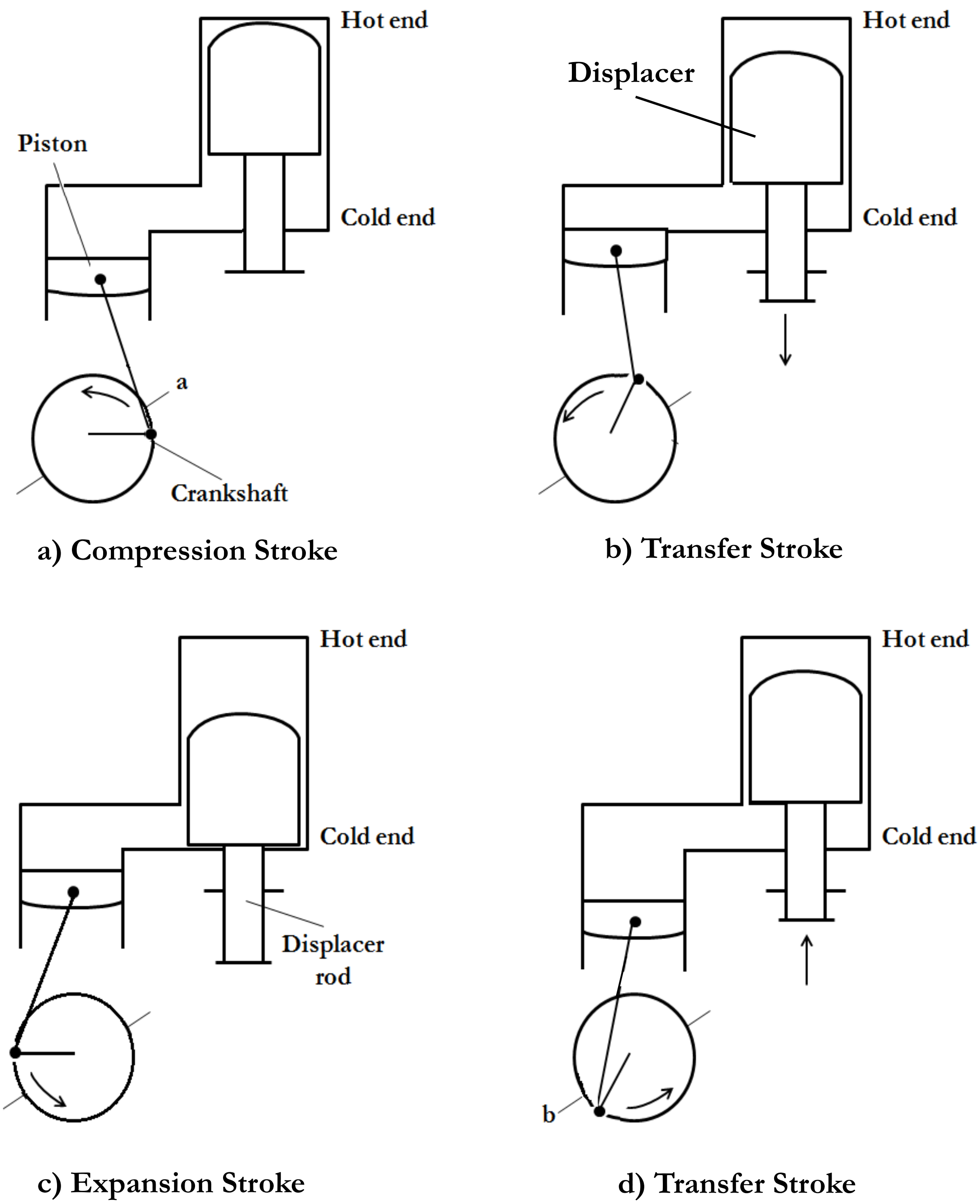

Figure 3.2 – Schematic representation of overdriven mode operation of a modified Ringbom engine [14]. The modification relates to the omission of the port in the piston-cylinder wall, shown in **Figure 3.1**.

Figure 3.3 depicts the motion of the piston and of the displacer with time and shows the displacer dwell periods. With the operating temperatures remaining fixed and, consequently, the crankshaft speed being constant, these dwell periods ensure that the displacer moves in precisely the same way during each cycle. Therefore, the phase relationship between the displacer and piston remains constant during operation. The displacer dwell period changes when the speed of the shaft is altered. There exists a limiting speed in which dwell periods in the displacer motion disappear, and the engine will no longer operate in steady-state. This is termed the "*overdriven limit*" [15]. This limiting speed is a function of both design and operating parameters.

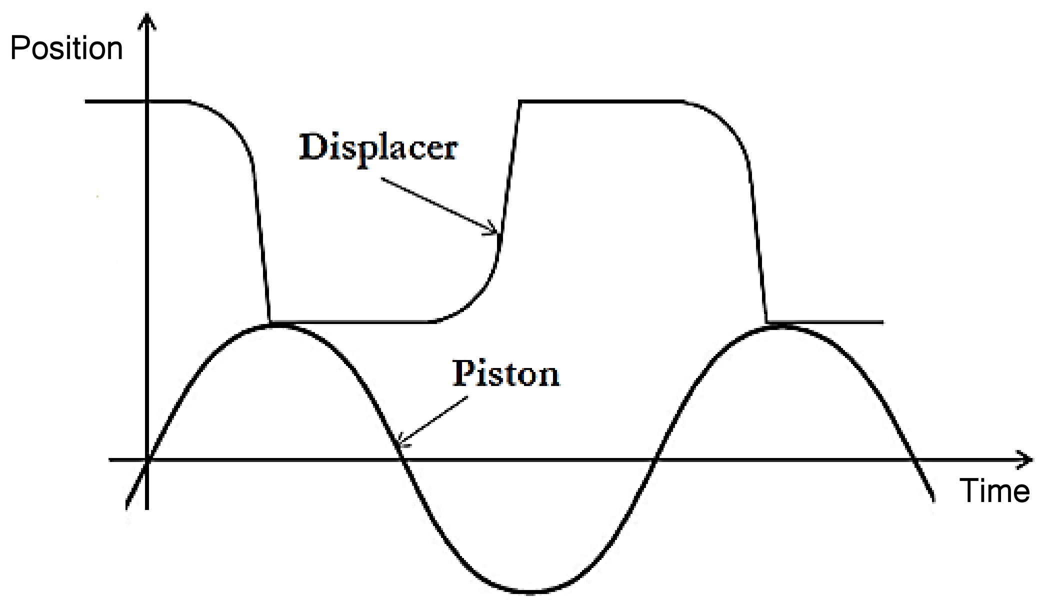

Figure 3.3 – Illustration demonstrating overdriven mode operation of a Ringbom engine. The horizontal portion of the displacer curve represents the displacer dwell periods [14].

3.2.2 Criterion for overdriven mode operation

In his paper, Senft [14] presents a simple and elegant condition for establishing the conditions that permit stable overdriven mode operation. This condition is stated in terms of two dimensionless parameters denoted γ and χ. In terms of these parameters, the model states that overdriven mode operation is possible if and only if

$$\gamma\chi + 1 \leq (\gamma\chi - 1)\exp(\pi\gamma). \tag{10}$$

Let us now review the assumptions and mathematical models that lead to this elegant criterion for overdriven mode operation.

3.2.3 Review of the derivation of the mathematical expression for overdriven mode operation

The mathematic expression for overdriven mode operation involves a significant number of parameters and is not trivial to derive. Therefore, a short review of the derivation of the expression for overdriven mode operation will be offered. To begin, the primary assumptions in Senft's analysis are listed below [14].

i) The Schmidt assumptions of isothermal spaces and uniform pressure are adopted. That is, each working space in the engine is isothermal in space and in time; and the pressure at any instant is spatially constant.
ii) The working fluid is an ideal gas.

iii) Within the engine, the mass of the working fluid is constant.
iv) Atmospheric pressure is constant and is equal to the internal pressure at the mid-stroke of the piston and of the displacer.
v) The displacer's length of travel is limited by unyielding stops, where the motion of the displacer halts instantaneously.
vi) Any bouncing that may occur at the stops is neglected.
vii) Any other force on the displacer via collisions with the stops is assumed inelastic (the stops are considered to be unidirectional dissipative).
viii) The only force acting on the displacer, when not held against one of its stops, is the pressure applied by the working fluid.
ix) The workspace pressure is symmetrical. Therefore, the motion of the displacer is identical in each direction.
x) The motion of the piston is a sinusoidal function of time.
xi) Gravity is negligible.
xii) The volume occupied by the displacer rod is negligible.
xiii) A circular geometry is assumed for both the piston and the displacer.
xiv) The engine configuration is the one shown in **Figure 3.4**.
xv) Frictional forces are negligible.

The model for the isothermal regions of the engine considers the expansion and compression volumes, and the pressure variation in these regions. The pressure is modeled as a function of the position of the displacer. The linear pressure model assumes a best linear approximation of the pressure at the position of the displacer and position of the piston, $x_D = 0$ and $x_P = 0$, respectively. The positions of the displacer and piston are referenced from their mid-stroke positions. The schematic of the engine, shown in **Figure 3.4**, highlights some of the important variables and their points of reference.

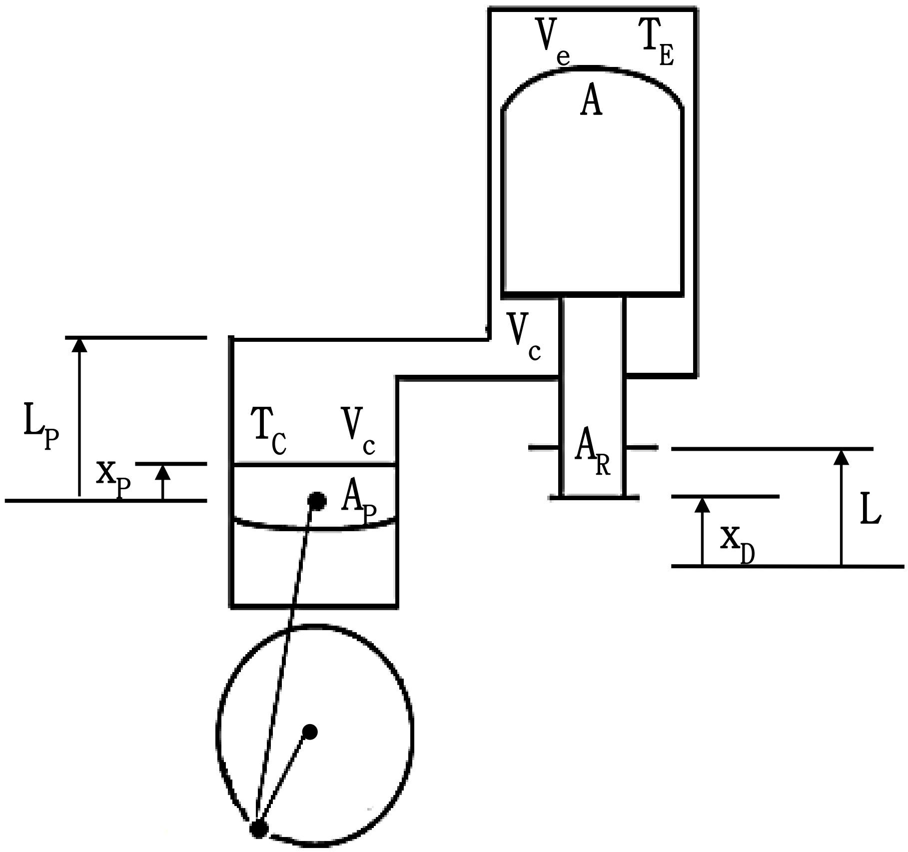

Figure 3.4 – Schematic of the Ringbom engine showing some of the important variables used in the mathematical statements of the model. The reference position of a few of the variables is presented also. A is the cross-sectional area of the displacer, A_P is the cross-sectional area of the piston, A_R is the cross-sectional area of the displacer rod, L_P is the amplitude of the motion of the piston, L is the maximum amplitude of the motion of the displacer, x_P is the position of the piston at time t, x_D is the position of the displacer at time t, V_e is the instantaneous volume of the expansion space, V_c is the instantaneous volume of the compression space, T_E is the temperature of the working fluid in the expansion space, and T_C is the temperature of the working fluid in the compression space [14].

The model used the equations for instantaneous expansion and compression space volume, with the application of the ideal gas law, to obtain the best linear approximation pressure function [14]. The expression for the volume of the instantaneous expansion space,

$$V_e = A(L - x_D), \tag{11}$$

was coupled with the equation for the volume of the instantaneous compression space,

$$V_c = (A - A_R)(L + x_D) + A_p(L_P - x_P) \tag{12}$$

along with the ideal gas law,

$$p = MR\left[\frac{V_e}{T_E} + \frac{V_c}{T_C} + \frac{V_D}{T_D}\right]^{-1} \tag{13}$$

to achieve a function for pressure which is given by

$$p = \frac{MRT_C}{A(1 - \tau - \rho)x_D - A_P x_P + AL(1 + \tau - \rho + \lambda\kappa + \sigma)} = p(x_D, x_P). \tag{14}$$

In these expressions, A is the cross-sectional area of the displacer; A_P is the cross-sectional area of the piston; A_R is the cross-sectional area of the displacer rod; L_P is the amplitude of the motion of the piston; L is the maximum amplitude of the motion of the displacer; x_P is the position of the piston at time, t; x_D is the position of the displacer at time, t; V_e is the instantaneous volume of the expansion space;

V_c is the instantaneous volume of the compression space; V_D is the volume of the dead space; T_E is the temperature of the working fluid in the expansion space; T_C is the temperature of the working fluid in the compression space; T_D is the temperature of the working fluid in the dead space; p is the instantaneous pressure of the working fluid; M is the mass of the working fluid; R is the gas constant of the working fluid; τ is the ratio of the temperature of the compression space to the temperature of the expansion space (T_C/T_E); ρ is the ratio of the area of the displacer rod to the area of the displacer (A_R/A); λ is the ratio of the amplitude of the motion of the piston to the maximum amplitude of the motion of the displacer (L_P/L), κ is the ratio of the area of the piston to the area of the displacer (A_P/A); $\sigma = \tau' V_D / AL$; and τ' is the ratio of the temperature of the compression space to the temperature of the working fluid in the dead space (T_C/T_D), and $\Delta p = p(x_D, x_P) - p(0,0)$ is the difference in pressure across the displacer rod.

The best linear approximation for the pressure function was obtained using the assumption that the external gas pressure is constant and equal to the internal gas pressure at the midstroke positions. Replacing Δp by its best linear approximation at (0,0), the expression for the pressure function is

$$\Delta p(x_D, x_P) = -C_0(1 - \tau - \rho)x_D + C_0 \kappa x_P \tag{15}$$

where $C_0 = \frac{MRT_C}{AL^2(1+\tau-\rho+\lambda\kappa+\sigma)^2}$ is a constant linked to various engine operating and geometrical parameters.

The next step involved the analysis of the motion of the displacer. The only force acting on the displacer while it is in motion is the pressure force which is given by

$$F_{Pressure} = A_R \Delta p(x_D, x_P). \tag{16}$$

This expression is combined with Newton's second law to obtain the equation of motion for the displacer as

$$\ddot{x}_D = -\left(\frac{A_R}{M_D}\right) \Delta p(x_D, x_P) \tag{17}$$

where M_D is the mass of the displacer assembly. Also, the motion of the piston is assumed to be time-harmonic; hence,

$$x_P = L_P \sin \varpi t \tag{18}$$

where ω is the angular velocity of the crankshaft.

Therefore, with equations (15), (16), and (18) substituted into equation (17), the differential equation describing the motion of the displacer is given by

$$\ddot{x}_D - Kx_D = -K\frac{\kappa}{1-\tau-\rho}L_P \sin \varpi t \tag{19}$$

where $K = \frac{A_R}{M_D}(1-\tau-\rho)C_0$ is a constant [14]. Thus far, the expressions necessary to obtain a linear, second-order differential equation for the motion of the displacer were not overly complicated. The steps can be easily followed and reproduced for use in one's own design of an engine. The general solution to the equation of motion of the displacer is

$$x_D = a \exp\left(\sqrt{K}t\right) + b \exp\left(-\sqrt{K}t\right) + \frac{\lambda\kappa}{1-\tau-\rho}\frac{KL}{K+\varpi^2}\sin \varpi t \tag{20}$$

where *a* and *b* are constants that depend on the initial conditions. These constants arise through solving the homogenous solution to the linear, second-order differential equation (19). Then, using the method of undetermined coefficients, the particular solution to equation (19) is obtained. The suitable initial conditions given by Senft [14] for the constants, *a* and *b*, are $x_D = L$ and $\dot{x}_D = 0$ when $t = t_o$, where

$$t_o = \frac{1}{\varpi}\arcsin\frac{1-\tau-\rho}{\lambda\kappa}. \tag{21}$$

Equation (20) can be simplified to yield an expression for the motion of the displacer that can be expressed as

$$x_D = \frac{L\varpi^2}{K + \varpi^2}(\frac{1}{2}(1 - \gamma\chi)\exp\left(\sqrt{K}(t - t_0)\right) + \frac{1}{2}(1 + \gamma\chi)\exp\left(-\sqrt{K}(t - t_0)\right) + \beta\gamma^2 \sin \varpi t) \tag{22}$$

where $\gamma = \frac{\sqrt{K}}{\omega}$, $\chi = \sqrt{\beta^2 - 1}$, and $\beta = \frac{\lambda\kappa}{1-\tau-\rho}$.

This equation is a function of the two primary dimensionless parameters, γ and χ. However, the equation is still too complex to offer a simple understanding to the effects of changing certain parameters of the engine. To gain additional insight, equation (22) must be further reduced. For overdriven mode operation, the displacer must reach its travel limit before some time interval, I, and the pressure force changes signs. Hence, $x_D(t) = - L$ before the end of the time interval, t_I, as illustrated in **Figure 3.5**.

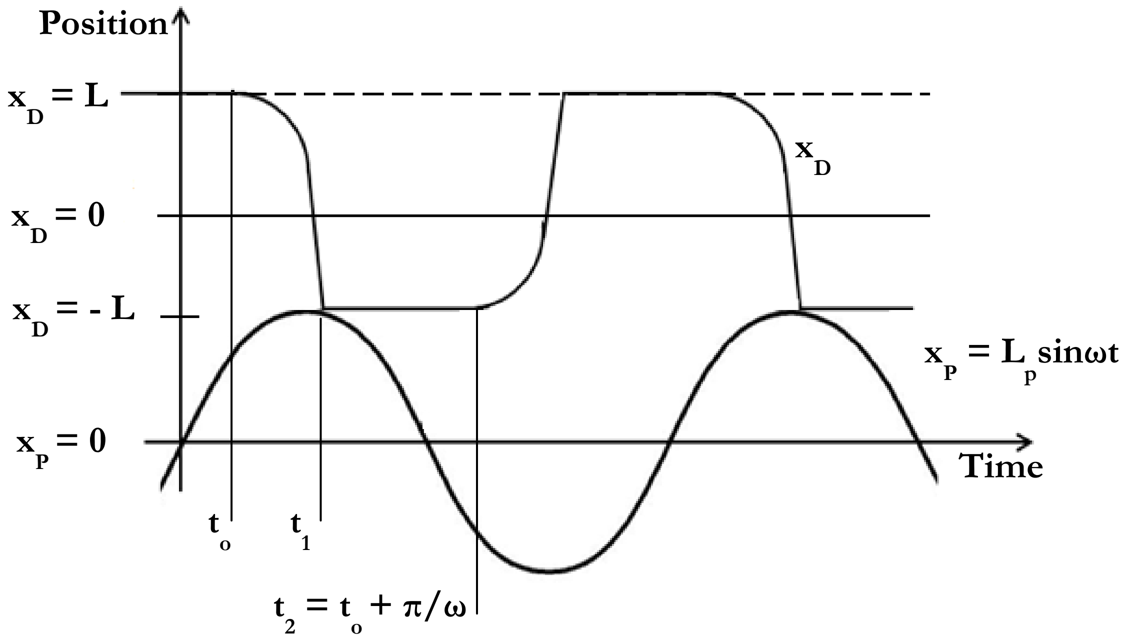

Figure 3.5 – Graph representing the motion of the displacer and the motion of the piston with time [14]. The horizontal space in the motion of the displacer curve signifies the dwell period of the displacer.

The equality $x_D(t) = - L$ can be rewritten as

$$x_D\left(t_o + \frac{\pi}{\varpi}\right) \leq -L \, . \tag{23}$$

The above expression, in its current form, seems simple without offering much information about designing for a Ringbom engine operating in overdriven mode operation. However, when the expression is simplified, it actually offers significant information regarding an initial design of an engine. With the help of *Appendix 2* in [15] – this can also be found in the appendix of this thesis –, equation (23) can be simplified further to give the statement of overdriven mode operation, as described in Eq. (10), where only two dimensionless parameters are involved.

The simplicity of this expression is slightly deceptive because γ and χ involve a multitude of variables. The secondary equations involved in $\gamma = \frac{\sqrt{K}}{\omega}$ and $\chi = \sqrt{\beta^2 - 1}$ are listed below [14].

a) $K = \frac{A_R}{M_D}(1 - \tau - \rho)C_0$

b) $C_0 = \frac{MRT_C}{AL^2(1+\tau-\rho+\lambda\kappa+\sigma)^2}$

c) $\beta = \frac{\lambda\kappa}{1-\tau-\rho}$

Of course, other variables and dimensionless parameters are involved in these secondary expressions. However, these include simple and obtainable geometric and operating parameters. **Table 3.1** presents the operating parameters, geometric parameters, and constants involved in the model. There are no arbitrary or free parameters involved in Senft's model, nor are there any parameters to account for friciton or dissipation losses [14]. Using a spreadsheet containing all these variables becomes a useful tool when implementing the model to design a Ringbom engine.

Table 3.1 – A table listing the classification of the parameters involved in Senft's model [14].

Geometric Parameters	Operating Parameters	Variables Involving Both Geometric & Operating Parameters	Universal Constants
A	p	β	R
A_P	Δp	C_o	
A_R	T_C	γ	
L	T_D	K	
L_P	T_E	σ	
x_D	ω	τ_o	
x_P	τ	χ	
V_c	τ'		
V_D			
V_e			
M			
M_D			
λ			
κ			
ρ			

Even though many parameters are involved in γ and χ, the advantage of having the expression of overdriven mode operation boil down to only two dimensionless parameters is that this mode of operation can be represented in the regime of a γ-χ plane, where the equation for the curve is

$$\chi = \frac{1}{\gamma}\frac{e^{\pi\gamma}+1}{e^{\pi\gamma}-1}. \tag{24}$$

The curve of this expression is shown in **Figure 3.6**, where the shaded area above the curve is the region of overdriven mode operation.

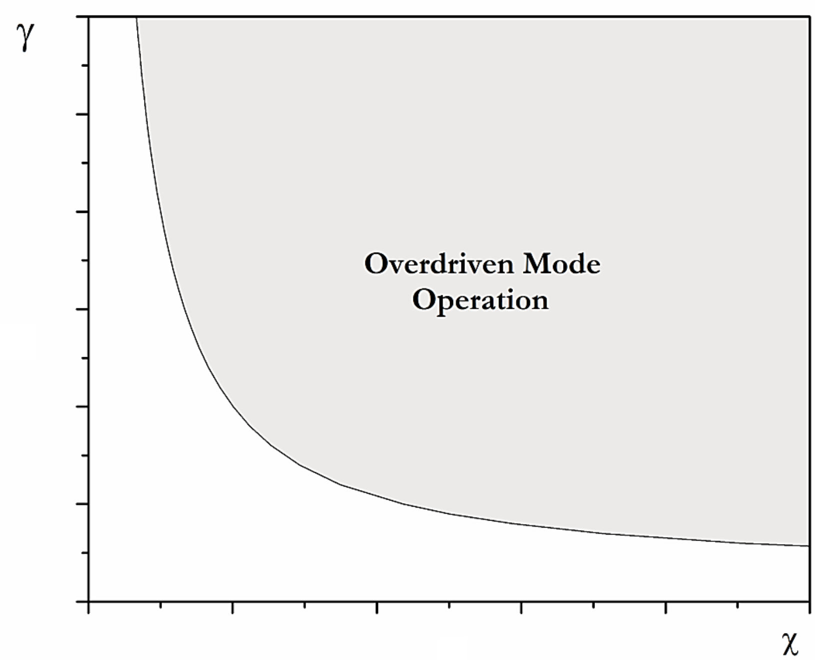

Figure 3.6 – Graphic representation of overdriven mode operation in the γ-χ plane [14].

Knowing the target geometry, operating temperatures and the speed of the shaft of a certain design of an engine, one can determine whether a point (χ, γ) will lie in the shaded region or on the boundary curve of **Figure 3.6**; in both cases, that engine is capable of sustaining overdriven mode operation. Additionally, one can correlate the locus of this point in the γ-χ plane with changes in design and operating parameters to determine if these changes will affect the operation of the engine. Therefore, the design of a Ringbom engine can be greatly simplified with the use of the model. Although additional simplifications and a thorough background knowledge of mathematics is required to fully understand the model and put it into use, it is a relatively simple initial tool for designing a Ringbom engine. For that reason, the next step of the thesis was to use the model by Senft [14] to design and analyze a Ringbom engine of the same size at the PT2-FBCP engine.

3.3 Designing a Ringbom engine using Senft's model

Several attempts were made using Senft's model [14] to design a Ringbom engine of the same size as the PT2-FBCP engine. The reference points for all the values of the parameters in the model were the engine geometries and operating conditions of the PT2-FBCP engine. Various geometries and operating conditions were input into the equations of the model to determine an appropriate design for a mesoscale Ringbom engine. According to the model, a Ringbom engine with a total volume of the engine of approximately 85 cm^3 would run steadily with a ΔT ranging from 25 ^oC to 60 ^oC. **Figure 3.7** shows a prediction of where a mesoscale Ringbom engine, roughly the same size at the PT2-FBCP engine, would be located in the operating space of overdriven mode operation, if running under ideal conditions, according to the analytical model described in the paper by Senft [14]. It is assumed that the cold temperature remains near to room temperature, that is, approximately 25 ^{o}C. The temperatures of the hot side of the engine are predicted to range from 50 ^{o}C to 90 ^{o}C. The lower temperature of the hot side is limited to 50 ^{o}C based on the experiences with the PT2-FBCP engine. The higher temperature of the hot side is limited by the predictions of the model, where it was determined that a hot side temperature higher than 90 ^{o}C would bring the point (χ,γ) outside the region of stable overdriven mode operation. From **Figure 3.7**, the equation $\gamma = \frac{\sqrt{K}}{\omega}$, and the insight provided by the paper by Senft [14], it can be seen that if an engine runs in overdriven mode operation at some speed, ω, it will operate in this mode for all speeds lower than ω. This is true because decreasing ω increases γ but leaves χ unaffected. In addition, there is an upper limit on the value of ω for each χ, namely the ω corresponding to the γ on the boundary curve [15].

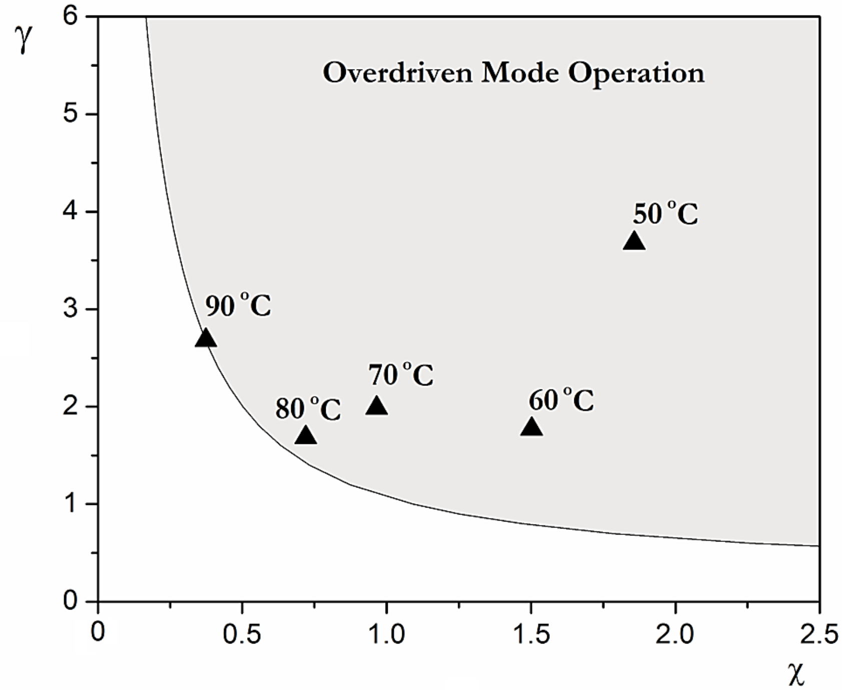

Figure 3.7 – Graph showing the prediction of performance, using Senft's model, of a mesoscale Ringbom engine, similar in size to the PT2-FBCP engine, operating in overdriven mode operation. Hot side input temperatures from 50 ^{o}C to 90 ^{o}C are predicted to allow the engine to operate in overdriven mode operation.

Low ΔT Ringbom engines are considered special because there is an upper limit on $T_{H,}$ where higher temperatures of the hot side of the engine decrease the overdriven limit. In addition, at temperatures above this limit, it was noted that the displacer locks and the engine will not operate [15].

The task now was to transform the gamma-type Stirling engine, the PT2-FBCP, to a Ringbom engine. It was decided that the PT2-FBCP engine would be used as the foundation for a Ringbom engine; that is, some of its components would be reused in the Ringbom engine design. More specifically, the piston-cylinder assembly, along with the flywheel and its mechanical linkages, would not be disassembled. It would be reused in the design of the new engine. Then, the metamorphosis of the PT2-FBCP engine to the Ringbom engine began with the investigation of the most influential geometric parameters affecting overdriven mode operation.

It is important to note that β must have a value greater than one for $\chi = \sqrt{\beta^2 - 1}$ to have an existing numerical value. It must also be greater than one such that the swept volume of the piston is sufficient to unlatch the displacer from its hot end and cold end dwell positions and push the displacer into motion [15]. Hence, if $\beta \leq 1$, the engine will not run. This dimensionless parameter, β, was further broken down into its components to determine which of its variables had effects on operating conditions. To ensure that β had a value greater than one, the dimensionless components of the latter were examined, where

$$\beta = \frac{\lambda\kappa}{1 - \tau - \rho} = \frac{(\frac{L_P}{L})(\frac{A_P}{A})}{1 - \frac{T_C}{T_E} - \frac{A_R}{A}}. \tag{25}$$

First, the denominator was inspected to conclude what values it could possibly assume. In the case of the PT2-FBCP engine for which geometric values of the

Ringbom engine will be based, τ and ρ should have a numerical value less than or equal to one. Thus, the denominator should have a value between zero and one. For the numerator, $\lambda\kappa$, it was noted that

$$L_P << L \tag{26}$$

and

$$A_P << A \tag{27}$$

leaving $L_P/L < 1$ and $A_P/A < 1$. The numerator, consequently, is less than one. Then, with the numerator assuming a value less than one, it was concluded that

$$\lambda\kappa > 1 - \tau - \rho \tag{28}$$

for β to have a value greater than one. The numerical value of the numerator could be made greater than that of the denominator through careful design of the geometry of the engine.

It became clear that the area of the displacer and dimensions of the displacer chamber were the most important factors affecting stable operation and those which would give β a suitable value for χ to exist. As such, the mathematical model was used to predict a suitably sized displacer and pin-point the displacer chamber dimensions, all the while remaining as true as possible to the size of the tested PT2-FBCP engine. The operating temperature range and speeds of the shaft input into the model were those of the PT2-FBCP engine. It was appropriate to use the same temperature ranges as a guideline for modeling since low temperature differential operation is desired. Also, it was appropriate to use the speeds obtained from testing the gamma-type Stirling engine because, "the mathematical analysis developed [...] will rigorously show that the Ringbom will operate in the overdriven mode over the entire speed range from zero (or, in practice, from the minimal operating speed determined by the flywheel, the condition of the engine, etc.) up to the limiting speed where the dwell periods just disappear, i.e. the *overdriven limit*" [15].

By inserting the engine geometry and operating conditions noted from experiments of the PT2-FBCP engine into the Ringbom model equations, it was clear that increasing the area of the displacer proved to make matters worse in terms of β resulting in a number less than 1. The decrease in β led further away from stable overdriven mode operation. Therefore, decreasing the area of the displacer was the direction in which to make changes. A decrease in the area of the displacer to one third of the original of the PT2-FBCP engine showed that β was above 1 – leading χ to have an existing value in the γ-χ plane – and that a Ringbom engine with a displacer of this area would run in overdriven mode operation. Now that the displacer area was set, the displacer chamber configuration was finalized. The only alteration to the displacer chamber was that it was made smaller in diameter, leaving only a 1 mm all-around gap for the working fluid to pass. The chamber height remained unchanged.

3.4 Modifying the gamma-type PT2-FBCP engine into a Ringbom engine

The deconstruction of the PT2-FBCP engine and the fabrication of the Ringbom engine, denoted from now onward as the RingStir-L^3, began by removing the displacer chamber from the aluminum plates, disconnecting the displacer rod from the flywheel, and removing the displacer itself from the PT2-FBCP engine assembly. The aluminum base and top plates were reused in the new design of the RingStir-L^3, as well as the nylon screws. The new displacer was made from high-temperature resistant polyester filter felt instead of balsa wood. It was chosen because the material is very light, similar in mass to balsa wood; it has a high-temperature resistance; it was easier to manipulate at one third of the area of the original displacer; and the air pockets in the meshing served as a regenerator because there was not sufficient surface area to insert foam for a regenerator. The displacer chamber was made from clear, high-temperature resistant vinyl. A clear material was chosen because of the necessity to visualize the mechanisms of the displacer during analysis. The top portion of the engine was not disassembled as the piston and flywheel configuration were of the right size to be reused in the RingStir-L^3 engine. With the top unit held together, the engines remained at a comparable size. **Figure 3.8** shows the components used in the RingStir-L^3 engine design.

Figure 3.8 – Photograph showing the relative size of the components of the RingStir-L^3 engine.

A transparent high-temperature resistant epoxy was chosen as a sealant for the displacer chamber. The engine was difficult to construct due to the fact that the displacer chamber needed to be hermetically sealed. The nylon screws offered little aid in putting pressure on the top and bottom plate to hold the engine tightly together. Once the engine was finally assembled, testing began.

3.5 Testing the RingStir-L^3 engine

Before the testing began of the completely assembled RingStir-L^3 engine on a heated surface, it was demonstrated that the components of the engine functioned as they should. That is, with the engine sitting on a flat surface without any heat source, the flywheel was set in motion. The displacer, which is free from any mechanical linkages, oscillated in its chamber. However, the oscillation only occurred over a few millimeters of the length of the displacer chamber. Questioning whether gravity could be the culprit of the minor oscillations, the RingStir-L^3 engine was held horizontally at its side, and the flywheel was set in motion. Now the displacer demonstrated oscillations spanning the full distance of the displacer chamber. Therefore, it was demonstrated that the mechanical components of the engine were functioning.

The next step was to determine whether the engine would operate on the ΔT that the model predicted would lead to overdriven mode operation. Testing began in much the same way as it did for the PT2-FBCP engine. The temperature range for testing was set for 50 ^{o}C to 90 ^{o}C in ten degree increments. The engine was to be placed on a hot plate and heated to a desired temperature before force-starting the flywheel into motion. The hotplate was heated to a desired temperature to within 2 ^{o}C. Two thermocouples were used to record the initial temperature of the base and hot plate. The room temperature was also recorded using the thermocouples and compared to the thermostat display. These two thermocouples were then taped to each base and top plate. The engine was then placed on the hot plate and allowed to heat up to the hot plate temperature before being force-started – since the Ringbom engine, much like the Stirling engine, is not self-starting.

When the engine's base plate reached the desired temperature, the flywheel was pushed to start the piston in motion. With the flywheel in motion, both piston and displacer moved from pressure and working fluid forces. However, not long after the engine was started, it ceased to operate. The effect of gravity was one problem causing the breakdown of the engine's performance and sustainability. It was also evident that the force of gravity was a problem since the displacer only oscillated through a few millimeters of its displacer chamber height even when being placed on a heat source. Because the displacer was not moving through its full range of motion, the working fluid was not being oscillated from the hot side of the chamber to the cold side, and vice versa, to create any substantial effect in the engine cycle. In addition to gravity being a major force against the motion of the displacer, the thermal expansion of the displacer rod became an important issue. The thermal expansion of the rod caused friction when passing through the brass displacer rod gland. The mechanical friction loss was too great to be overcome by working fluid pressure. This was negligible in the PT2-FBCP engine since the flywheel inertia and connecting rod had enough force to move the displacer.

In an attempt to optimize performance and diminish the negative effect that gravity held on the displacer of the engine, it was decided to test the engine while it was held horizontally on the heat source. **Figure 3.9** and **Figure 3.10** show the engine being held in this configuration.

Figure 3.9 – Photograph showing the setup for the testing of the RingStir-L^3 engine, where engine is held horizontally.

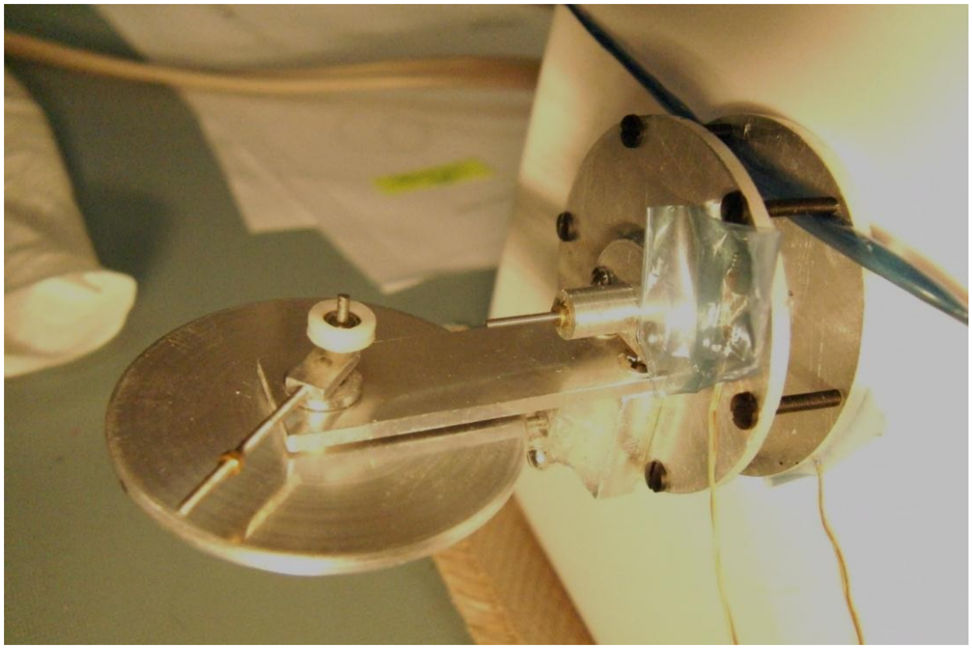

Figure 3.10 – Photograph showing the RingStir-L^3 engine being tested horizontally to diminish effect of gravity on displacer. In addition, the photograph shows clearly that the displacer is no longer attached to the flywheel.

The testing of the engine proceeded in exactly the same way as before. Once the flywheel was set in motion, the piston and displacer functioned only for a short while and engine operation ceased, similar to the vertical setup. However, it was noted that the displacer now travelled the full length of its chamber. Hence, one improvement was made to the engine.

Again, however, the thermal expansion of the displacer rod was a great problem. The thermal expansion of the displacer rod was an issue that was not easily avoided or solved. Silicone spray and lubricants were used in an attempt to minimize friction between the displacer rod and gland. However, without avail, the friction was too much to overcome. Changing the material to one with a lower coefficient of thermal expansion would have been an option or using a piston-cylinder configuration would have been viable, as well, for this size of engine. Though, tending toward a microscale engine design calls for one to get rid of the piston-cylinder configurations. Therefore, in an effort to steer away from adding more piston-cylinder mechanisms, this route was disregarded. In the context of miniaturizing the engine for potential microelectromechanical systems (MEMS) based applications, using a lubricant is not a possible solution to the problem of friction forces. Therefore, it was decided that the solution would have to be an altered configuration of the displacer of the engine.

3.6 Discussion

The model by Senft [14] predicted that a Ringbom engine of approximately the same size as the PT2-FBCP engine would operate in overdriven mode operation, as depicted in **Figure 3.7**. Conversely, the effect of gravity and mechanical friction losses inhibited the engine from running in stable steady-state. The RingStir-L^3 engine had the potential to function because a check was completed to determine whether the engine components functioned. However, the engine was not capable of operating in steady-state overdriven mode operation while placed on a heat source. The thermodynamic cycle of the engine was not completed and the dynamics were compromised due to frictional losses and inhibiting forces. The model appears to be a good planning tool for the initial design of a Ringbom engine. However, a higher-order model should be adopted afterward to refine the engine to account for gravity and frictional losses.

Moving towards miniaturizing the engine and entering a MEMS realm, one would want to reduce the number of moving parts and find material to work with that can be manipulated and utilized in MEMS processing and fabrication. The goal of reducing friction applies to a multitude of applications, but it is assuredly the case when trying to move toward creating any MEMS device. Hence, moving away from piston-cylinder arrangements and toward solid membrane structures seems to be the direction one should take when designing for microfabricated engines.

Chapter 4: Summary and future work

4.1 Overview of motivation and approach

The main motivation for the work presented in this thesis was to explore the utility and feasibility of developing miniaturized Stirling engines for waste heat recovery. The ultimate long-term goal is to develop robust, high-performance engines with a volume of about 1 cm^3 to power the operation of portable devices and wireless networks of sensors. The fundamental thermodynamic principles of the Stirling cycle are well known. However, many challenges must be solved before this cycle can be implemented using small-scale engines. Many aspects of the design, manufacture, operation, performance, and reliability are affected by size. For example, the geometries, materials, and shapes that are used for larger (macroscale) Stirling engines may not be suitable for their miniaturized counterparts. The design space must be revisited and extended to identify optimal geometries and materials, while taking into account the stringent constraints by the current state of micromachining technologies. In addition, the standard methods used for assembling and testing large-scale engines cannot be directly employed on small-scale engines. New experimental methods must be developed to probe the performance and reliability of miniaturized engines.

4.2 Guidelines for miniaturization

The challenge of miniaturizing Stirling engines can be approached using two basic guidelines. The first arises from a fundamental feature of the Stirling cycle. Regardless of any other consideration, the engine requires a difference in temperature between two of its components in order to implement the Stirling cycle. Sustaining this difference becomes increasingly more difficult as the size of the engine shrinks. Therefore, the type of Stirling engine that is selected for miniaturization must belong to the class of low temperature differential (LTD) engines.

The second guideline arises out of practical considerations. The field of MEMS has progressed rapidly over the past two decades and many sophisticated micromachines have been built for numerous applications [25]. However, there are major differences in the approach to design and manufacture between large-scale systems (macrosystems) and MEMS. Macrosystems commonly employ a wide range of mechanisms using rigid bodies that are connected using linkages. In contrast, there are few methods for assembling and joining the components of MEMS. As a consequence, these miniaturized systems typically use relatively simple compliant mechanisms that are built and assembled simultaneously. Therefore, the design of microscale Stirling engines must rely upon simple mechanisms that require few linkages.

4.3 Mesoscale gamma-type Stirling engine

As a first step, a mesoscale (palmtop size) gamma-type Stirling engine was designed, assembled, and tested. This type of engine was selected because the literature suggested that gamma-type engines are capable of operating with relatively low temperature differences, ΔT. The complexities associated with micromachining were eliminated by using conventional techniques for machining all components.

This mesoscale engine was instrumented and tested to assess its performance. The engine was capable of operating with relatively low ΔT ranging from 23 ^{o}C to 100 ^{o}C. Under these conditions, the steady-state angular velocity of the flywheel ranged between 200 RPM and 500 RPM, which implies a kinetic energy of a few millijoules.

4.4 Mesoscale Ringbom-type Stirling cycle engine

The second step was to explore the operation of the engine and to transform the gamma-type Stirling engine into a Ringbom engine. This transformation is accompanied by a reduction in the number of linkages in the engine, which is an attractive feature for further miniaturization, and guided by a detailed analytical model developed by Senft [14]. Specifically, the mechanical linkage connecting the displacer to the flywheel was removed to convert the gamma-type Stirling engine into a Ringbom engine.

Senft's model offers a prediction of the conditions under which the Ringbom engine is capable of operation in overdriven mode [14]. However, when the mesoscale engine was tested under these conditions, it was found that it could not sustain steady-state overdriven mode operation because of friction between the displacer rod and the displacer rod gland. Such frictional forces are not taken into consideration in the model.

This experience highlights the challenge of developing models for Stirling engines. The goal was relatively modest – that is, simply to predict whether or not the engine could operate in overdriven mode. But even this could not be accomplished because of the complicating effects of friction in the engine. Accounting for such dissipative and surface-related phenomena is expected to become more important, and also more challenging, as the size of the engine decreases.

4.5 Towards microscale MEMS-based Stirling engines

The experience gained with the mesoscale gamma-type Stirling and Ringbom engines offers some guidelines for further miniaturization. There is a huge opportunity for harvesting waste heat for portable power. A survey of the literature shows that several approaches – Rankine micro-engines, thermoelectric devices, and pyroelectric devices – are being investigated for developing efficient miniaturized devices that can convert waste heat into mechanical and electrical energy [26-28].

Many questions remain open at this early stage in the development of these devices. The relative merits and drawbacks of the various approaches are not yet clear. Moreover, the feasibility of developing efficient and reliable micro-devices for harvesting waste heat has yet to be established. Therefore, there is value in exploring each of these options to establish the effects of size on performance and reliability, and to develop guidelines and methods for analysis and design. The remaining sections of this chapter explore these ideas in the context of microscale Stirling engines.

4.5.1 Setting limits on size

First and foremost, for a Stirling cycle engine to operate, a difference in temperature must exist between the hot side and cold side of the engine. Maintaining this difference becomes particularly difficult when the scale becomes so small that only a few millimeters separates each side of the engine. A scaling analysis of regenerative heat engines suggests that the distance between the hot side and cold side should not be smaller than 1 mm [19]. Beyond this size, the efficiency of the engine reduces precipitously. This sets a fundamental limit on the size of a microscale Stirling engine.

4.5.2 Designing within the constraints of microfabrication technologies

The approaches used for micromachining and microfabrication are radically different from those used to machine large-scale components. In turn, these differences impose stringent constraints on the type of shapes, materials, and structures that can be used in the design of microscale Stirling engines.

The assembly line is a standard feature of conventional manufacturing. That is, each device is manufactured by serial assembly of modular components. These components are usually manufactured by methods that use mechanical contact for shaping materials; examples of such methods include stamping, forging, and milling. These techniques permit the machining of complex three-dimensional geometries using a variety of ceramic, metallic, and polymeric materials.

In contrast, the standard approach for micromachining relies upon selective corrosion (also called *etching*) for shaping materials. In addition, there are no standard methods for assembly and joining. That is, there is no counterpart for techniques such as welding, brazing, and riveting for microscale components. Therefore, micromachines are usually built layer-by-layer so that the components are machined and assembled simultaneously. This approach is usually implemented in a massively parallel manner. A single operation can affect thousands (in some cases, tens of thousands) of devices and components.

The creative use of micromachining methods has led to the design of numerous sophisticated devices. For example, the Digital Micromirror Device (DMD) manufactured by Texas Instruments contains a million micromirrors on a chip with an area of a few square centimeters [29]. This device is commonly used for projection and displays. The motion of each mirror can be controlled using electrostatic actuation of torsional hinges. **Figure 4.1** shows a schematic illustration of two mirrors contained in the DMD.

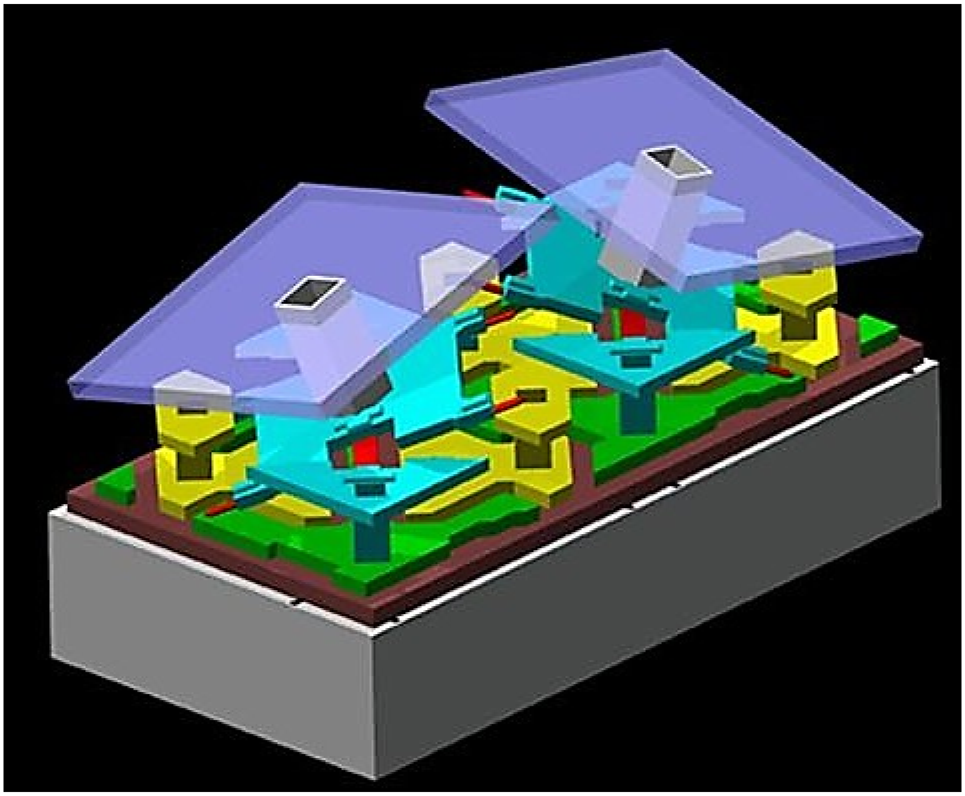

Figure 4.1 – Illustration of the Texas Instruments Digital Micromirror Device (DMD) showing the complexities of the three-dimensional structure [29].

If a microscale Stirling engine is to be manufactured by this set of microfabrication processes, then it is necessary to devise a layer-by-layer strategy to design. This approach has been adopted for the design of miniaturized engines implementing the Brayton and Rankine cycles [30, 31]. In addition, it is necessary to minimize the number of linkages, and to use compliant mechanisms, for the Stirling engine.

4.6 Future work: Miniaturization of free-piston Stirling engines

The experience gained with mesoscale gamma-type Stirling and Ringbom engines, and the foregoing considerations of scale effects, lead to the conclusion that the *free-piston configuration* is ideally suited for miniaturization. This configuration requires few linkages. Indeed, it is possible to implement free-piston Stirling engines using compliant membranes as the only moving parts [26, 32]. Thus, the design can be implemented in a layer-by-layer manner, thereby making it compatible with microfabrication methods. The design and development of miniaturized free-piston Stirling engines will be explored in a trilateral collaboration between Université de Savoie in France, Université de Sherbrooke and McGill University.

Appendix

A. CAD illustration of the components of the PT2-FBCP engine

The CAD illustration presented below, **FIGURE A.1**, was created by François Bisson and Christopher Palucci. Alterations were made to the drawing to provide improved clarity.

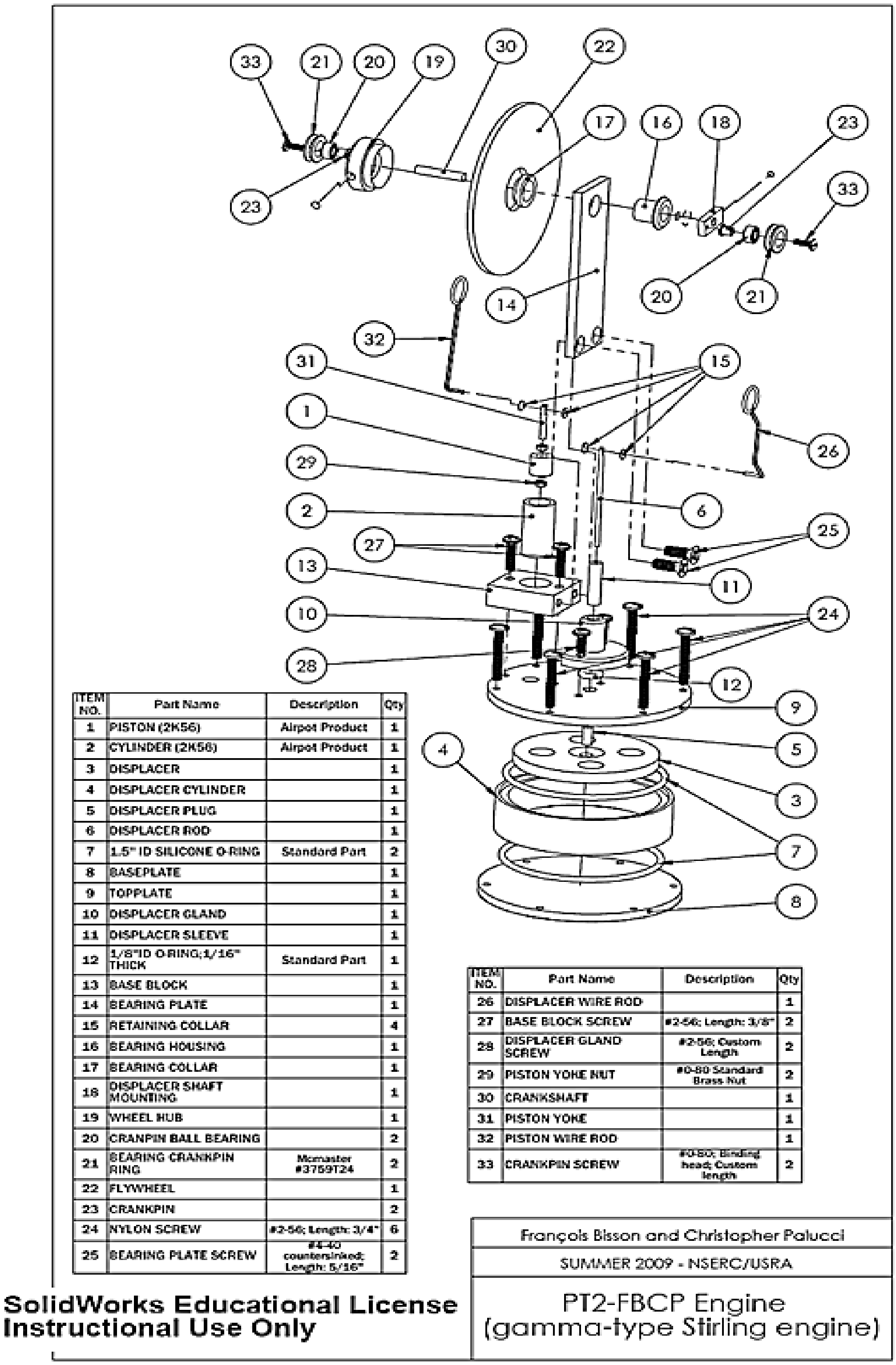

ITEM NO.	Part Name	Description	Qty
1	PISTON (2K56)	Airpot Product	1
2	CYLINDER (2K56)	Airpot Product	1
3	DISPLACER		1
4	DISPLACER CYLINDER		1
5	DISPLACER PLUG		1
6	DISPLACER ROD		1
7	1.5" ID SILICONE O-RING	Standard Part	2
8	BASEPLATE		1
9	TOPPLATE		1
10	DISPLACER GLAND		1
11	DISPLACER SLEEVE		1
12	1/8"ID O-RING;1/16" THICK	Standard Part	1
13	BASE BLOCK		1
14	BEARING PLATE		1
15	RETAINING COLLAR		4
16	BEARING HOUSING		1
17	BEARING COLLAR		1
18	DISPLACER SHAFT MOUNTING		1
19	WHEEL HUB		1
20	CRANPIN BALL BEARING		2
21	BEARING CRANKPIN RING	Mcmaster #3759T24	2
22	FLYWHEEL		1
23	CRANKPIN		2
24	NYLON SCREW	#2-56; Length: 3/4"	6
25	BEARING PLATE SCREW	#4-40 countersinked; Length: 5/16"	2

ITEM NO.	Part Name	Description	Qty
26	DISPLACER WIRE ROD		1
27	BASE BLOCK SCREW	#2-56; Length: 3/8"	2
28	DISPLACER GLAND SCREW	#2-56; Custom Length	2
29	PISTON YOKE NUT	#0-80 Standard Brass Nut	2
30	CRANKSHAFT		1
31	PISTON YOKE		1
32	PISTON WIRE ROD		1
33	CRANKPIN SCREW	#0-80; Binding head; Custom length	2

Figure A.1 – CAD illustration of the exploded view of the PT2-FBCP engine.

B. Data tables from experimental testing of PT2-FBCP engine

The tables containing the data results obtained from the testing of the PT2-FBCP engine are presented below. The tables show the temperature of the hot side of the engine, the temperature of the cold side of the engine and the corresponding speed of the shaft for the temperature differential.

Table A.1 – Table showing the results from testing the PT2-FBCP engine.

Target $T_{hotplate}$ °C	Actual $T_{hotplate}$ °C	Final $T_{coldplate}$ °C	Temperature Difference	Speed of Shaft (RPM)
50	54.3	30.2	24.1	152
50	54.4	31.5	22.9	177
50	54.1	33.8	20.3	153
50	54.5	31.3	23.2	157
50	54.6	31	23.6	176
50	54.6	31.7	22.9	147
50	54.7	31.3	23.4	170
50	54.4	31.5	22.9	161
60	60	32.2	27.8	272
60	59.9	35.8	24.1	191
60	59.3	37.1	22.2	190
60	60.1	30.2	29.9	198
60	60.5	31.3	29.2	161
60	60.8	31.6	29.2	196
60	60	32.7	27.3	196
60	60.1	33.3	26.8	200
70	72.3	36	36.3	281
70	72.7	37.1	35.6	227
70	72.3	34.4	37.9	257
70	73.2	37.4	35.8	147
70	72.2	34.5	37.7	225

70	72.7	37.5	35.2	196
70	72	40	32	192
70	72.8	33.6	39.2	200
80	80.3	38.9	41.4	356
80	80.3	34.2	46.1	296
80	80.3	38.7	41.6	243
80	80.8	37.4	43.4	173
80	80.9	35.5	45.4	261
80	80.3	38.9	41.4	209
80	80.7	42.3	38.4	247
80	80.9	33.9	47	225
90	89.3	40.9	48.4	243
90	89.5	36.8	52.7	352
90	89.4	36.5	52.9	286
90	89.7	39.4	50.3	180
90	89.4	36.6	52.8	254
90	89.1	41.6	47.5	273
90	90.1	36.9	53.2	261
90	90.1	35.7	54.4	217
100	100.5	46.8	53.7	228
100	99.6	39.1	60.5	359
100	100.1	41.7	58.4	265
100	100.6	41	59.6	240
100	100.7	37.6	63.1	316
100	100.5	38	62.5	321
100	100	37.1	62.9	267
100	100.1	34.7	65.4	265
110	110.8	47.4	63.4	206
110	110.7	37	73.7	368
110	111.4	42.8	68.6	277
110	110.4	43.6	66.8	310
110	110.3	37.3	73	327
110	110.1	39.4	70.7	346
110	110.3	36.5	73.8	286
110	110.3	39.4	70.9	310

120	121.6	44	77.6	392
120	121.9	39.8	82.1	395
120	122.2	44.6	77.6	400
120	122.2	43.8	78.4	286
120	120.1	45.2	74.9	400
120	122.4	44.3	78.1	360
120	122.4	44.4	78	340
120	122.3	41.2	81.1	265
130	133.2	52.2	81	348
130	133.5	45.2	88.3	497
130	133.4	45.2	88.2	474
130	133.1	40.8	92.3	327
130	133.1	44.8	88.3	360
130	133.1	45	88.1	409
130	132.7	47.6	85.1	391
130	132.2	45	87.2	305
140	140.3	50.9	89.4	521
140	140.9	48.1	92.8	522
140	139.9	45.4	94.5	409
140	140.2	43.8	96.4	462
140	139.9	46.7	93.2	400
140	139.9	41.5	98.4	546
140	140	44.8	95.2	367
140	139.9	47.2	92.7	367
150	150.3	57.7	92.6	530
150	150	51.3	98.7	505
150	150	46.7	103.3	529
150	149.5	48.9	100.6	529
150	149.9	51.7	98.2	529
150	149.9	47.1	102.8	529
150	149.9	45.5	104.4	439
150	149.9	48.5	101.4	391

C. Derivation showing the equivalency of expressions in Senft's Model

In the model presented by Senft [14], the proof was absent showing that the inequalities (1) and (22) are equivalent. The expressions below [15], show that the inequalities are same:

$$x_D\left(t_o + \frac{\pi}{\varpi}\right) \leq -L \tag{22}$$

$$\frac{L\varpi^2}{K+\varpi^2}\left(\frac{1-\gamma\chi}{2}e^{\sqrt{K}\frac{\pi}{\varpi}} + \frac{1+\gamma\chi}{2}e^{-\sqrt{K}\frac{\pi}{\varpi}} + \beta\gamma^2\sin(\varpi t_o + \pi)\right) \leq \ -L$$

$$\frac{1}{2}(1-\gamma\chi)e^{\pi\gamma} + \frac{1}{2}(1+\gamma\chi)e^{-\pi\gamma} - \beta\gamma^2\sin\varpi t_o \leq -\frac{K+\varpi^2}{\varpi^2}$$

$$\frac{1}{2}(1-\gamma\chi)e^{\pi\gamma} + \frac{1}{2}(1+\gamma\chi)e^{-\pi\gamma} - \beta\gamma^2\frac{1}{\beta} \leq -\gamma^2 - 1$$

$$(1-\gamma\chi)e^{\pi\gamma} + 2 + (1+\gamma\chi)e^{-\pi\gamma} \leq 0$$

$$[(1-\gamma\chi)e^{\pi\gamma} + (1+\gamma\chi)][1+e^{-\pi\gamma}] \leq 0$$

$$(1-\gamma\chi)e^{\pi\gamma} + (1+\gamma\chi) \leq 0$$

$$(1+\gamma\chi) \leq -(1-\gamma\chi)e^{\pi\gamma}$$

$$\gamma\chi + 1 \leq (\gamma\chi - 1)e^{\pi\gamma} \tag{1}$$

References

[1] G. Walker, *Stirling-Cycle Machines*, Oxford Univeristy Press, Ely House, London, 1973.

[2] http://www.stirlingengine.com, *American Stirling Company*, Accessed October 17, 2011.

[3] P. Lombardi and P. Sutton, "Automotive Stirling engine development: Program status," *Proceedings of the 8th Energy Technology Conference*, pp. 646-661, 1981.

[4] W. K. Tabata, "Automotive Stirling engine development program - A success," 04999320, NASA, Cleveland, USA, 1987.

[5] http://en.wikipedia.org/wiki/gotland_class_submarine, *Gotland class submarine*, Accessed October 17, 2011.

[6] H. Nilsson, "Air independent power systems for autonomous submarines " *Ocean Engineering and the Environment - Conference Record*, pp. 42-55, 1985.

[7] G. Hong, Z. Chen, C. Yan, G. Xu, T. Wang and F. Guo, "Characteristic experiments of a space Stirling cryocooler," *Proceedings of the International Conference on Energy Conversion and Application (ICECA'2001),* pp. 1047-1051, 2001.

[8] B. C. Howard, http://www.thedailygreen.com/environmental-news/latest/stirling-solar-power-46012108, *Can Stirling Engines and a Record-Holding Company Deliver Massive Solar Power Gains?,* Accessed November 9, 2011.

[9] G. Walker and J. R. Senft, *Lecture Notes in Engineering 12: Free Piston Stirling Engines*, Springer-Verlag, Berlin, 1985.

[10] M. J. Moran and H. N. Shapiro, *Fundamentals of Engineering Thermodynamics*, John Wiley and Sons Ltd, West Sussex, England, 2006.

[11] D. G. Thombare and S. K. Verma, "Technological development in the Stirling cycle engines," *Renewable and Sustainable Energy Reviews*, vol. 12, pp. 1-38, 2008.

[12] I. Urieli and D. M. Berchowitz, *Stirling Cycle Engine Analysis*, Adam Hilger Ltd, Techno House, 1984.

[13] B. Kongtragool and S. Wongwises, "Investigation on power output of the gamma-configuration low temperature differential Stirling engines," *Renewable Energy*, vol. 30, pp. 465-476, 2005.

[14] J. R. Senft, "A mathematical model for Ringbom engine operation," *Journal of Engineering for Gas Turbines and Power*, vol. 107, pp. 590-595, 1985.

[15] J. R. Senft, *Ringbom Stirling Engines*, Oxford University Press, New York, USA, 1993.

[16] M. Ball, http://www.vector1media.com/spatialsustain/hp-and-shell-team-on-a-massive-wireless-sensor-network-for-exploration.html, *HP and Shell Team on a Massive Wireless Sensor Network for Exploration,* Accessed October 14, 2011.

[17] Y. B. Turkogullan, N. Aras, I. K. Altinel and C. Ersoy, "Optimal placement, scheduling, and routing to maximize lifetime in sensor networks," *Journal of the Operational Research Society*, vol. 61, pp. 1000-12, 2010.

[18] N. Nakajima, K. Ogawa and I. Fujimasa, "Study on microengines: miniaturizing Stirling engines for actuators and heatpumps," *Sensors and Actuators*, vol. 20, pp. 75-82, 1989.

[19] R. B. Peterson, "Size limits for regenerative heat engines," *Microscale Thermophysical Engineering*, vol. 2, pp. 121 - 131, 1998.

[20] D. A. Wang and K. H. Chang, "Electromagnetic Energy Harvesting From Flow Induced Vibration," *Microelectronics Journal*, vol. 41, pp. 356-364, June 2010.

[21] J. R. Senft, *An Introduction to Low Temparature Differential Sitrling Engines*, Moryia Press, River Falls, WI, 1996.

[22] http://www.omega.com/temperature/pdf/hhm290.pdf, Accessed October 21, 2011.

[23] http://www.airtechintl.com, Accessed October 21, 2011.

[24] http://support.casio.com/pdf/001/exf1_mf_fd_110808_e.pdf, *Casio digital camera EX-F1 user's guide*, pp. 184, Accessed October 21, 2011.

[25] S. D. Senturia, *Microsystem design*, Kluwer Academic Publishers, Boston, 2001.

[26] F. Formosa, A. Badel and E. Arroyo, " Electromagnetic generator design for membrane micro Stirling engine," *Power MEMS 2010*, 2010.

[27] M. Liamini, H. Shahriar, S. Vengallatore and L. G. Frechette, "Design methodology for a rankine microturbine: Thermomechanical analysis and material selection," *Journal of Microelectromechanical systems*, vol. 20, pp. 339-351, 2011.

[28] J. Yu and M. Ikura, "Experimental study on applying the pyroelectric effect to low-grade waste-heat power recovery," *Journal of Xi'an Jiaotong University*, vol. 38, pp. 28-31, 2004.

[29] J. D. Jackson, http://www.optics.rochester.edu/workgroups/cml/opt307/spr05/john/, *A visual analysis of a Texas Instruments digital micromirror device*, Accessed November 17, 2011.

[30] L. G. Frechette, C. Lee, S. Arslan and Y. C. Liu, "Design of a microfabricated rankine cycle steam turbine for power generation," *2003 ASME International Mechanical Engineering Congress,* vol. 5, pp. 335-344, 2003.

[31] A. Mehra, Z. Xin, A. A. Ayon, I. A. Waitz, M. A. Schmidt and C. M. Spadaccini, "A six-wafer combustion system for a silicon micro gas turbine engine," *Journal of Microelectromechanical systems*, vol. 9, pp. 517-27, 2000.

[32] F. Fabien, "Nonlinear dynamics analysis of a membrane Stirling engine: Starting and stable operation," *Journal of Sound and Vibration*, vol. 326, pp. 794-808, 2009.